

Unification of Exceptional Points and Transmission Peak Degeneracies in a Highly Tunable Magnon-Photon Dimer

Alexander S. Carney,¹ Juan S. Salcedo-Gallo,¹ Salil K. Bedkihal,¹ and Mattias Fitzpatrick^{1,2}

¹*Thayer School of Engineering, Dartmouth College, 15 Thayer Drive, Hanover, New Hampshire 03755, USA*

²*Department of Physics and Astronomy, Dartmouth College, 6127 Wilder Laboratory, Hanover, New Hampshire 03755, USA*

(Dated: July 24, 2025)

Exceptional points (EPs), spectral singularities arising in non-Hermitian dynamical systems, have drawn widespread attention for their potential to enhance sensor capability by leveraging characteristic square-root frequency splitting. However, the advantages of EP sensors have remained highly contested, primarily due to their inherent hypersensitivity to fabrication errors and loss of precision arising from eigenbasis collapse, quantified by the Petermann noise factor. Recently, it has been suggested that practical sensor implementations should instead utilize transmission peak degeneracies (TPDs), which exhibit square-root transmission splitting while maintaining a complete eigenbasis, avoiding the Petermann noise around EPs. This work presents a microwave magnon-photon dimer with near-universal tunability across all relevant parameters, which we use to survey a surface of EPs and TPDs experimentally, including a newly introduced phase-non-reciprocal TPD. We demonstrate that two-dimensional EP and TPD configurations based on coupled oscillators can be unified into a general theory and experimental framework utilizing synthetic gauge fields, which we present and validate through careful experiments on six representative TPDs. We also introduce practical figures of merit to quantify the performance and robustness of TPDs beyond just the Petermann noise factor. Our formalism and experimental methods unify previous EP and TPD configurations, and may lead to the widespread realization of robust TPD-enhanced sensors.

Over the past decade, numerous proposals and experiments have investigated the potential of EPs to enhance sensing [1–6]. Near an EP, eigenvalues exhibit a characteristic square-root response when subjected to perturbations in specific system parameters [7]. Despite their promise and early demonstrations [8], practical implementations of EP sensors have encountered considerable technical hurdles. Specifically, EP-based sensors require precise, isolated parameter tuning in high-dimensional parameter spaces, where even slight deviations due to fabrication errors rapidly diminish the enhanced response, a phenomena known as parameter hypersensitivity. More fundamentally, however, the eigenvector collapse at EPs—responsible for their characteristic square-root response—inherently enhances noise. This intrinsic noise enhancement at EPs, quantified by the divergence of the Petermann noise factor [9, 10], fundamentally challenges achievable improvements in signal-to-noise ratio for EP-based sensors [11]. Consequently, the viability of frequency-splitting-based EP sensors has been the subject of contentious debate [9, 12–17].

To circumvent this fundamental noise-response trade-off inherent to EPs, recent advances have shifted attention toward distinguishing intrinsic eigenspectrum degeneracies from transmission spectrum degeneracies observed in experiments. Recently, it was shown that transmission extrema can exhibit square-root frequency splitting in the proximity of a transmission spectrum degeneracy while maintaining a complete eigenbasis [5, 18, 19]. Such transmission spectrum degeneracies manifest as dips in reflection or peaks in transmission, but this work will exclusively focus on so-called transmission *peak* degeneracies (TPDs) without loss of generality. Clarifying the distinction between EPs and TPDs is essential to re-

solving the debate regarding whether TPD-based sensors can practically fulfill the original promise of EP-enhanced sensing. While earlier efforts have comprehensively studied EPs, previous investigations of TPDs have received less attention and lack a unified theoretical framework.

Previous experimental platforms for studying EPs and TPDs most commonly include microcavities operating in the optical regime [8, 20–22], electrical circuits, including superconducting circuits, in the RF regime [5, 19, 23–26], or cavity magnonics in the microwave regime [27, 28]. Cavity magnonics exploits strong magnon-photon coupling to enable quantum sensing by hybridizing spin excitations with electromagnetic fields [29]. Crucially, the coupling phase between magnonic and photonic modes acts as an additional control knob that can be used to alter the coupling structure and modify the system dynamics [30–32]. Specifically, phases play a crucial role in “loop-coupled” geometries, where they combine to form effective U(1) gauge fields [33] and can be used to realize tunable coherent and dissipative couplings [34, 35]. These synthetic gauge fields in cavity magnonics can also enable non-reciprocal interactions by breaking symmetries, as demonstrated in a generalized Hatano-Nelson model [36, 37].

This work introduces a flexible theoretical and experimental framework that unifies two-dimensional coupled-oscillator-based EP and TPD configurations, establishing a foundation for future TPD-based sensors. We present a tunable microwave magnon-photon dimer with independent control of resonance frequencies, dissipation rates, coupling strengths, and coupling phase. We use these control knobs to survey a surface of EPs and TPDs embedded within the six-dimensional parameter space, traversed using a synthetic gauge field on the coupling term,

$Je^{i\phi}$, effectively forming a non-Hermitian beam splitter [38]. We demonstrate three sets of EPs and TPDs and study how the TPDs move with parameter choice to locations with a complete—or even orthogonal—eigenbasis. Our platform flexibility may enable the optimization of sensor characteristics based on figures of merit introduced in Sec. III A. The formalism, platform, and experimental methods presented here are versatile testbeds for TPD sensors and general non-Hermitian physical phenomena.

I. EXPERIMENTAL ARCHITECTURE

Our experimental architecture is a coupled magnon-photon system, forming a dimer between the lowest harmonic of a three-dimensional microwave cavity [39] and a magnon mode realized using a yttrium iron garnet (YIG) sphere of radius 1 mm. In the presence of a static magnetic field, electron spins in YIG collectively precess about the field axis, forming a resonance analogous to ferromagnetic resonance (FMR) (for more details, see Supplementary Information). The Larmor frequency is $f_y = \mu_B B_z / 2\pi$, where μ_B is the Bohr magneton, consistent with the simplified Kittel formula for a uniformly magnetized sphere [40, 41]. The YIG mode is coupled to using two orthogonal wire bonds that encircle the YIG sphere. Without the YIG, the loops are electromagnetically isolated, preventing power transmission between them. When the YIG is inserted, its spin resonance enables microwave coupling between the input and output loops only at frequencies near the Larmor frequency. Therefore, the oscillator hosting the YIG passes signals around f_y , with full-width-half-maximum κ_y , while attenuating others, manifested as a characteristic Lorentzian transmission spectra [42].

The magnon and photon modes are spatially separated by approximately one meter [43]. Coupling between the modes is split into independent coupling paths using SMA microwave coaxial cables (Fig. 1a). Following previous work, we place a tunable directional amplifier in each coupling path to symmetrically tune the coupling strength J , and include a phase shifter ϕ in one arm to introduce phase non-reciprocity in the coupling [35] (Methods). This phase non-reciprocity does not necessarily break reciprocity in the strict electromagnetic sense, but produces direction-dependent phase evolution, effectively producing a synthetic gauge field [33]. The resulting complex coupling coefficient, $Je^{i\phi}$, is tunable across the full range $\phi \in [0, 2\pi)$ while preserving the coupling magnitude, allowing access to distinct coupling regimes. At $\phi = 0$, or reciprocal phase coupling, the system exhibits level repulsion, characterized by an avoided crossing whose gap increases with the coupling strength J (Fig. 1b,c,f,g). Modifying the average dissipation rate, $\bar{\kappa} = (\kappa_c + \kappa_y)/2$, modifies the linewidths of the hybridized modes while preserving the repulsion behavior (Fig. 1f,g). At $\phi = \pi$, or anti-reciprocal phase cou-

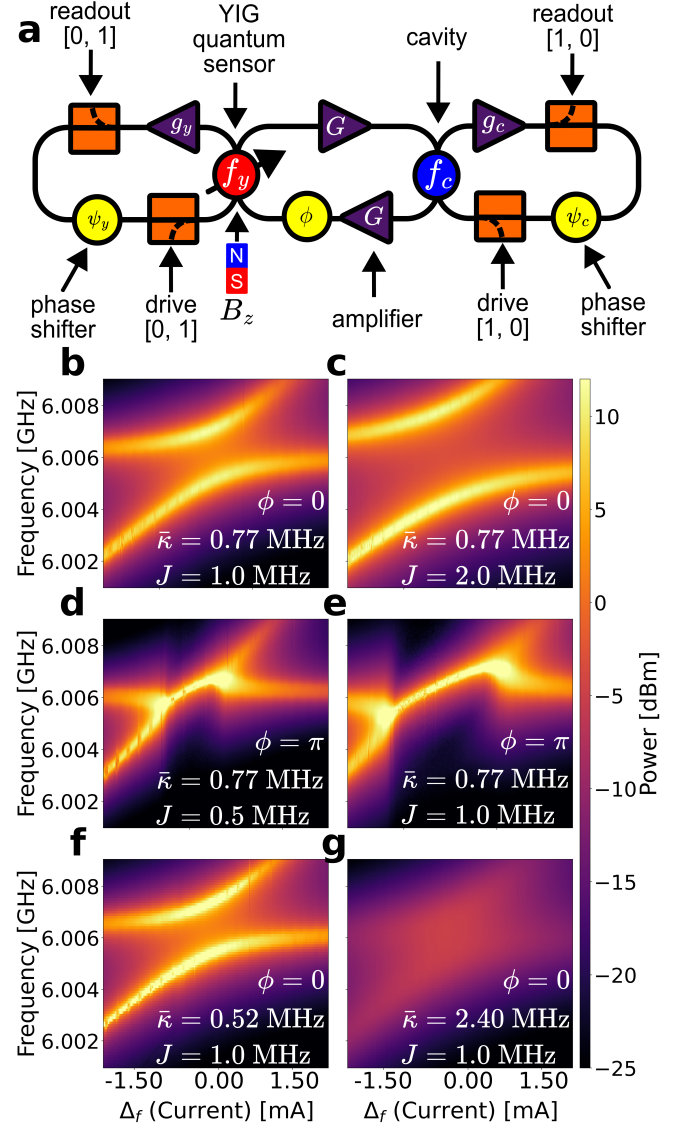


Figure 1. **Tunable magnon-photon architecture.** **a**, Experimental schematic depicting coupling control parameters (G, ϕ), which determine the coupling strength J and coupling phase ϕ , and auxiliary control parameters ($g_c, g_y, \psi_c, \psi_y, B_z$), which control the mode parameters $f_c, f_y, \kappa_c, \kappa_y$. **b-g**, Transmission spectra as a function of current through an external electromagnet, which tunes the YIG frequency f_y through B_z and thereby controls the detuning between the modes. Data illustrate level repulsion ($\phi = 0$) (**b,c,f,g**) and level attraction ($\phi = \pi$) (**d,e**) for varying coupling strengths J and average dissipation rates $\bar{\kappa}$.

pling, level attraction is observed, where the hybridized modes coalesce and split as the individual frequencies are detuned [30] (Fig. 1d,e). The extent of the coalescence region increases with J , as expected. For all other phase values, such as $\phi = \pi/2$, the two couplings still share the same magnitude but their complex phases differ by an angle that cannot be removed by a single phase redefi-

dition or gauge transformation, resulting in true phase-non-reciprocal dynamics.

To complete the six-parameter control of the dimer, each mode is further equipped with a self-feedback loop consisting of a phase shifter with phase $\psi_{c,y}$ and an effective variable-gain amplifier with gain $g_{c,y}$ (Fig. 1a), where the subscripts (c, y) correspond to the cavity and YIG self-feedback loops, respectively. Adjusting $\psi_{c,y}$ and $g_{c,y}$ provides in-situ tuning of the mode frequency $f_{c,y}$ and dissipation rate $\kappa_{c,y}$. At each step during an experiment, we probe both modes individually with coupling disabled to extract $f_{c,y}$, $\kappa_{c,y}$ and uncertainties $\sigma(f_{c,y}), \sigma(\kappa_{c,y})$ (Methods). Furthermore, any desired f_y, κ_y can be attained using our regression-based parameter control system that optimally sets ψ_y, g_y (Methods). Figure 1 illustrates the complete experimental schematic (Fig. 1a) and various transmission experiments highlighting parameter control (Fig. 1b–g).

II. NON-HERMITIAN DYNAMICS

The dynamics of the dimer are modeled using a state space model, governed by the semiclassical equations of motion

$$\dot{\alpha} = \tilde{\mathbf{A}}\alpha + \mathbf{B}u, \quad (1)$$

$$\tilde{\beta}_{ss} = \left| \mathbf{C}\tilde{\mathbf{A}}^{-1}\mathbf{B}u \right|^2. \quad (2)$$

where $\tilde{\mathbf{A}}$ is the dynamical system matrix defined in Eq. 3, and $\alpha = [\alpha, m]^T$ denotes the complex coherent state amplitudes of the photon (α) and magnon (m) modes. $\mathbf{B} \in \{[1, 0]^T, [0, 1]^T\}$ is the drive vector, where $\mathbf{B} = [1, 0]^T$ ($\mathbf{B} = [0, 1]^T$) represents driving the cavity (YIG) with drive strength u . Complex mode amplitudes are measured by $\mathbf{C}\alpha$ with $\mathbf{C} \in \{[1, 0], [0, 1]\}$ the readout vector, $\mathbf{C} = [1, 0]$ ($\mathbf{C} = [0, 1]$) corresponds to reading out the cavity (YIG). $\tilde{\beta}_{ss}$ in Eq. 2 represents the steady state transmission spectrum, which is only valid when all real parts of the eigenvalues of $\tilde{\mathbf{A}}$ are negative. When $\tilde{\mathbf{A}}$ becomes unstable, amplifier saturation eventually curbs the runaway gain, leading to nonlinear phenomena reported in earlier work but not considered here [35].

In the rotating frame with respect to the drive frequency f_d , the system matrix generates dynamics and is given in nondimensionalized form by

$$\tilde{\mathbf{A}} = \begin{bmatrix} -i(\tilde{f}_c - \tilde{f}_d) - \frac{\tilde{\kappa}_c}{2} & -i \\ -ie^{i\phi} & -i(\tilde{f}_c - \tilde{f}_d - \tilde{\Delta}_f) + \left(\tilde{\Delta}_\kappa - \frac{\tilde{\kappa}_c}{2}\right) \end{bmatrix} \quad (3)$$

where $\tilde{f}_c = f_c/J$, $\tilde{\kappa}_c = \kappa_c/J$, etc., and $\tilde{\Delta}_f = \tilde{f}_c - \tilde{f}_y$, and $\tilde{\Delta}_\kappa = (\tilde{\kappa}_c - \tilde{\kappa}_y)/2$ (see Supplementary Information for derivation) [32].

A. Eigenspectrum Analysis

The eigenvalues $\tilde{\lambda}_\pm$ of the dynamical matrix $\tilde{\mathbf{A}}$ are given by

$$\tilde{\lambda}_0 = \left(\frac{\tilde{\Delta}_\kappa}{2} - \frac{\tilde{\kappa}_c}{2} \right) + i \left(\frac{\tilde{\Delta}_f}{2} - \tilde{f}_c + \tilde{f}_d \right), \quad (4)$$

$$\tilde{\Delta}_\lambda = \sqrt{-\tilde{\Delta}_f^2 + 2i\tilde{\Delta}_f\tilde{\Delta}_\kappa + \tilde{\Delta}_\kappa^2 - 4e^{i\phi}}, \quad (5)$$

$$\tilde{\lambda}_\pm = \tilde{\lambda}_0 \pm \frac{\tilde{\Delta}_\lambda}{2}. \quad (6)$$

where $\text{Re}(\tilde{\lambda})$ is related to dissipation or gain, and $\text{Im}(\tilde{\lambda})$ is related to oscillation frequency. This convention is opposite to the typical Hamiltonian-based formulation, but consistent with standard practice in input–output theory [35]. The quantity $\tilde{\Delta}_\lambda$ defines the complex spectral splitting between the eigenvalues. Figure 2 i(ii) depicts $|\text{Im}(\tilde{\Delta}_\lambda)|$ ($\text{Re}(\tilde{\Delta}_\lambda)$) on the $\tilde{\Delta}_\kappa$ - $\tilde{\Delta}_f$ plane.

EPs are defined by the coalescence of eigenvectors and eigenvalues. The mean diagonal Petermann noise factor, $\bar{K}_2 = \frac{1}{2}(K_{11} + K_{22})$, is used to quantify eigenvector non-orthogonality. $\bar{K}_2 = 1$ when eigenvectors are orthogonal, and diverges at EPs [10, 44, 45]. For $\tilde{\mathbf{A}}$ in Eq. 3, we find

$$\bar{K}_2 = \frac{\tilde{\Delta}_f^2 + \tilde{\Delta}_\kappa^2 + |\tilde{\Delta}_\lambda|^2 + 4}{2|\tilde{\Delta}_\lambda|^2}. \quad (7)$$

For a given $\phi \in [0, 2\pi)$, solving $|\tilde{\Delta}_\lambda| = 0$ for $\tilde{\Delta}_\kappa, \tilde{\Delta}_f$ simultaneously yields a continuous manifold of EPs in parameter space, called an exceptional surface [46], parameterized by

$$\tilde{\Delta}_\kappa = \pm 2 \cos\left(\frac{\phi}{2}\right), \quad \tilde{\Delta}_f = \pm 2 \sin\left(\frac{\phi}{2}\right). \quad (8)$$

At each value of ϕ , there are two EPs (“primary” and “other”), plotted in Fig. 2, where $\text{Re}(\tilde{\Delta}_\lambda) = \text{Im}(\tilde{\Delta}_\lambda) = 0$, with “primary” EPs investigated experimentally in Fig. 3. In the vicinity of EPs, \bar{K}_2 diverges, corresponding to noise enhancement at those parameter regimes [9, 47]. Moving away from the EPs in the $\tilde{\Delta}_\kappa$ - $\tilde{\Delta}_f$ plane reduces \bar{K}_2 , reaching a minimum value of $\bar{K}_2 = 1$ between the two EPs. This line of minimal \bar{K}_2 is the $\tilde{\Delta}_f$ axis for $\phi = 0$ (Fig. a.iii–iv), the $\tilde{\Delta}_\kappa$ axis for $\phi = \pi$ (Fig. b.iii–iv), and the line $\tilde{\Delta}_f = -\cot(\phi/2)\tilde{\Delta}_\kappa$ for all other values of ϕ , with $\tilde{\Delta}_f = -\tilde{\Delta}_\kappa$ at $\phi = \pi/2$ (Fig. c.iii–iv).

B. Transmission Spectrum Analysis

Transmission peak frequencies are found from the critical points of $\tilde{\beta}_{ss}$, obtained by solving $\frac{\partial}{\partial \tilde{f}_d}(\tilde{\beta}_{ss}) = 0$ for \tilde{f}_d . This condition yields a nonlinear equation for \tilde{f}_d ,

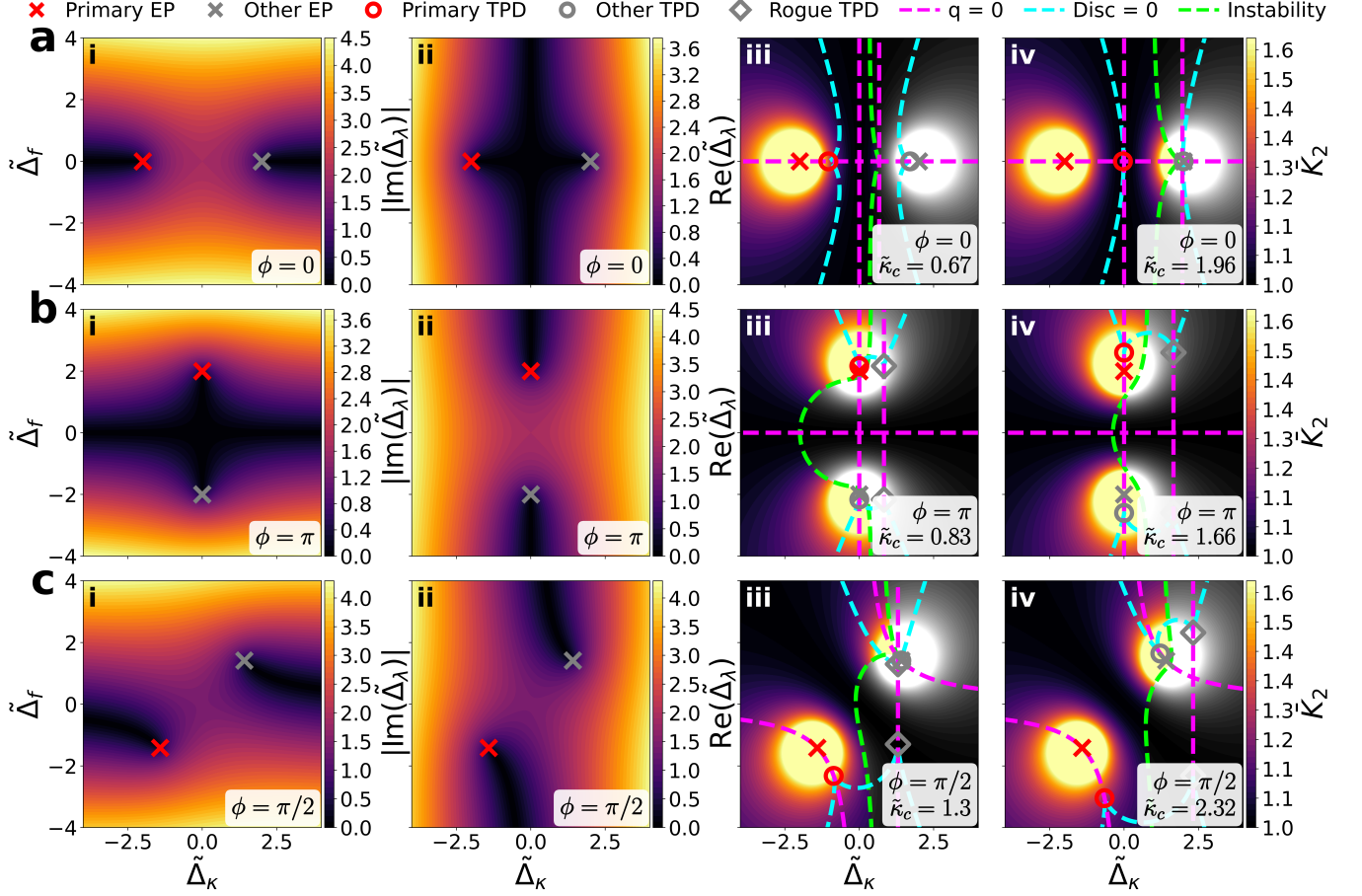


Figure 2. **Geometry of EPs and TPDs.** Parameter landscapes for $\phi = 0$ (a), $\phi = \pi$ (b), and $\phi = \pi/2$ (c). Eigenspectrum characteristics include absolute imaginary eigenvalue splitting $|\text{Im}(\tilde{\Delta}_\lambda)|$ (i), real eigenvalue splitting $\text{Re}(\tilde{\Delta}_\lambda)$ (ii), and mean diagonal Petermann factor \bar{K}_2 (iii-iv). Crosses are EPs, where $\text{Im}(\tilde{\Delta}_\lambda) = \text{Re}(\tilde{\Delta}_\lambda) = 0$ (i-ii), and \bar{K}_2 diverges (iii-iv) (\bar{K}_2 colorscale is clipped to 90th percentile). Transmission spectrum characteristics are determined by the contours in iii-iv, whose locations depend on $\tilde{\kappa}_c$. Chosen values of $\tilde{\kappa}_c$ match those used in experiment (Fig. 3). Cyan contours are $\text{Disc} = 0$ (discriminant of Eq. 9), separating the parameter space into single peak (between cyan contours horizontally) and two peak (outside cyan contours horizontally) regions. Magenta contours are $\tilde{q} = 0$ (Eq. 11). We select the $\tilde{q} = 0$ contour that crosses the primary EP and TPD as the independent variable in Fig. 3. Lime contours are $\text{Re}(\tilde{\Delta}_\lambda) = (\tilde{\kappa}_c - \tilde{\Delta}_\kappa)$, and separate the parameter space into stable (inferno colorscale) and unstable (gray colorscale) regimes (Eq. 2 is inapplicable in the unstable regime and not considered in this work). Circles represent TPDs associated with an EP (Primary EPs and TPDs, in red, are observed in Fig. 3), while diamonds represent TPDs not associated with an EP, referred to as rogue TPDs.

which can be expressed as a depressed cubic in terms of an auxiliary variable f of the form

$$0 = f^3 + \tilde{p}f + \tilde{q}, \quad (9)$$

$$\tilde{p} = \frac{(\tilde{\kappa}_c - \tilde{\Delta}_\kappa)^2 + \text{Re}(\tilde{\Delta}_\lambda^2)}{4}, \quad (10)$$

$$\tilde{q} = \frac{(\tilde{\kappa}_c - \tilde{\Delta}_\kappa) \text{Im}(\tilde{\Delta}_\lambda^2)}{8}. \quad (11)$$

Equation 9 can either admit a single real root, $\tilde{\nu}_0^{\text{Root}}$, or three real roots, $\tilde{\nu}_\pm^{\text{Root}}, \tilde{\eta}^{\text{Root}}$. All roots can be converted

into experimentally relevant extrema locations by

$$\tilde{\nu}_{\pm,0} = \tilde{\nu}_{\pm,0}^{\text{Root}} + \tilde{f}_c - \frac{\tilde{\Delta}_f}{2}, \quad (12)$$

$$\tilde{\eta} = \tilde{\eta}^{\text{Root}} + \tilde{f}_c - \frac{\tilde{\Delta}_f}{2}. \quad (13)$$

When Eq. 9 admits a single real root, $\tilde{\nu}_0$ is the single peak frequency. Otherwise, $\tilde{\nu}_\pm$ are the two peak frequencies, with $\tilde{\eta}$ representing the frequency of the local minima between the two peaks. The splitting between the peaks is $\tilde{\Delta}_\nu = \tilde{\nu}_+ - \tilde{\nu}_-$, analogous to $\tilde{\Delta}_\lambda$ from Eq. 5. The analysis of the roots of Eq. 9 is extensively studied in the Supplementary Information, including a closed form solution for

the peak locations using a trigonometric solution posed by François Viète in 1615 [48–50].

TPDs are defined by the coalescence of the two peak frequencies. Mathematically, we locate TPDs by solving $\text{Disc} = \tilde{q} = 0$ for $\tilde{\Delta}_f, \tilde{\Delta}_\kappa$ simultaneously, where Disc is the discriminant of Eq. 9. This surface of TPDs has a significantly more complicated solution than the exceptional surface in Eq. 8, and is fully parameterized in the Supplementary Information. The critical takeaway from this analysis is that the surface of TPDs is dependent on both $\tilde{\kappa}_c$ and ϕ . Depending on the choice of $\tilde{\kappa}_c$ and ϕ , there can be two, four, or six TPDs. This dependence on both parameters is further investigated with theory in Fig. 2 and experiment in Fig. 3.

To observe the symmetric square root splitting of eigenvalues and transmission peaks characteristic of EPs and TPDs, a path must be chosen in the $\tilde{\Delta}_\kappa$ - $\tilde{\Delta}_f$ plane, which becomes the independent variable that ensures symmetric square root splitting. This path is defined by the contour $\tilde{q} = 0$ and is plotted in Fig. 2iii, iv. Following \tilde{q} through the TPD ensures $\text{Re}(\tilde{\Delta}_\lambda) = 0$ throughout the sweep (Fig. 2ii), such that both peaks split with symmetric amplitudes. For any value of ϕ , there are always $\tilde{q} = 0$ contours that smoothly intersect both an EP and a TPD, which we probe using our experimental apparatus in Fig. 3. For $\phi = 0$, this experimental sweep path is the $\tilde{\Delta}_\kappa$ axis (Fig. 3a-b), or the $\tilde{\Delta}_f$ axis for $\phi = \pi$ (Fig. 3c-d). For intermediate values of ϕ , the sweep path becomes a hyperbola defined by $\tilde{\Delta}_\kappa \tilde{\Delta}_f = 2 \sin(\phi)$ (Fig. 2c.iii-iv), requiring simultaneous control of $\tilde{\Delta}_f$ and $\tilde{\Delta}_\kappa$ (Fig. 3e-f) (Methods).

When the sweep path $\tilde{q} = 0$ intersects an EP, the eigenvalues split with a square root profile, not necessarily observed in transmission. When $\tilde{q} = 0$ intersects the zero-discriminant contour $\text{Disc} = 0$, a TPD occurs and the transmission peaks split with a square root profile. When $\tilde{q} = 0$ intersects the instability contour, defined as $\text{Re}(\tilde{\Delta}_\lambda) = (\tilde{\kappa}_c - \tilde{\Delta}_\kappa)$ (Fig. 2iii-iv), the system becomes unstable, and the steady state transmission is no longer governed by Eq. 2. Remarkably, there can be up to 4 other TPDs on $\tilde{q} = 0$ contours that do not intersect EPs. We refer to these as rogue TPDs, which are depicted in Fig. 2iii-iv.

III. EXPERIMENTAL RESULTS

The locations of EPs and TPDs, denoted $\tilde{\Delta}_{f,\kappa}^{\text{EP}}, \tilde{\Delta}_{f,\kappa}^{\text{TPD}}$ with respect to the independent variable set by sweeping $\tilde{q} = 0$ are visualized in Fig. 3. We report the theory and results of EPs and TPDs explored at $\phi = 0, \pi, \pi/2$, with representative small and large $\tilde{\kappa}_c$ to survey the surface of EPs and TPDs. To ensure the validity of our linear model, we select “primary” EPs and TPDs that involve purely dissipative dynamics (Fig. 2).

The experimental methods are summarized here, and detailed in Methods. For each value of ϕ , we record J and use it to convert measured frequencies (such as Δ_f) to

nondimensionalized parameters (such as $\tilde{\Delta}_f$). Sweeps are initialized by setting $\tilde{\kappa}_c$ and specifying a $\tilde{\Delta}_f$ or $\tilde{\Delta}_\kappa$ range. A control system is used to follow a trajectory in $\tilde{\Delta}_f$ - $\tilde{\Delta}_\kappa$ space (Methods). For each step of a sweep, we independently probe each mode in isolation (by setting $J = 0$) and fit the isolated mode trace to a Lorentzian, extracting cavity (YIG) parameters $f_{c(y)}, \kappa_{c(y)}$ and $\sigma(f_{c(y)}), \sigma(\kappa_{c(y)})$ to obtain $\tilde{\Delta}_f, \tilde{\Delta}_\kappa, \sigma(\tilde{\Delta}_f), \sigma(\tilde{\Delta}_\kappa)$. Then, coupling is enabled ($J \neq 0$), and Eq. 2 is fit to the experimental data using $\tilde{\Delta}_\kappa$ and $\tilde{\Delta}_f$. All parameters are fit to Eq. 12 to extract $\tilde{\nu}_\pm$ data, reported in Fig. 3iii, with error bars representing uncertainty propagation from $\sigma(\tilde{\Delta}_\kappa), \sigma(\tilde{\Delta}_f)$.

For $\phi = 0$, we calibrate $J = 1.05$ MHz (Methods), and $\tilde{\Delta}_\kappa$ is swept while $\tilde{\Delta}_f = 0$, with $\tilde{\Delta}_\kappa^{\text{EP}} = \pm 2$, $\tilde{\Delta}_\kappa^{\text{TPD}} = \frac{\tilde{\kappa}_c}{2} \pm \frac{\sqrt{8 - \tilde{\kappa}_c^2}}{2}$, $\tilde{\Delta}_f^{\text{EP, TPD}} = 0$, provided $\tilde{\kappa}_c^2 - 8 \leq 0$. Figure 3a-b depicts the EP at $\tilde{\Delta}_\kappa^{\text{EP}} = -2$, with TPDs at $\tilde{\Delta}_\kappa^{\text{TPD}} = -1.04(1)$ for $\tilde{\kappa}_c = 0.67(1)$ (Fig. 3a) and $\tilde{\Delta}_\kappa^{\text{TPD}} = -0.04(4)$ for $\tilde{\kappa}_c = 1.96(1)$ (Fig. 3b). The peak locations, $\tilde{\nu}_\pm$, do not split at the EP, and even after they split at the TPD, they remain bounded by the imaginary eigenvalues (Fig. 3a.i, b.i). The instability transition occurs at $\tilde{\Delta}_\kappa^{\text{NL}} = \tilde{\kappa}_c$ for $\tilde{\kappa}_c \leq 2$, or $\tilde{\Delta}_\kappa^{\text{NL}} = \frac{\tilde{\kappa}_c^2 + 4}{2\tilde{\kappa}_c}$ for $\tilde{\kappa}_c > 2$. Figure 3a.i-iii shows $\tilde{\Delta}_\kappa^{\text{NL}} = 0.67(1)$.

For $\phi = \pi$, we calibrate $J = 1.13$ MHz, and $\tilde{\Delta}_f$ is swept while $\tilde{\Delta}_\kappa = 0$, with $\tilde{\Delta}_f^{\text{EP}} = \pm 2$, $\tilde{\Delta}_f^{\text{TPD}} = \pm \sqrt{\tilde{\kappa}_c^2 + 4}$, $\tilde{\Delta}_f^{\text{NL}} = \pm \sqrt{4 - \tilde{\kappa}_c^2}$, $\tilde{\Delta}_\kappa^{\text{EP, TPD, NL}} = 0$. Figure 3c-d depicts the EP at $\tilde{\Delta}_f^{\text{EP}} = +2$, with TPDs and instability transitions at $\tilde{\Delta}_f^{\text{TPD}} = 2.167(4)$, $\tilde{\Delta}_f^{\text{NL}} = 1.817(4)$ for $\tilde{\kappa}_c = 0.83(1)$ (Fig. 3c) and $\tilde{\Delta}_f^{\text{TPD}} = 2.598(7)$, $\tilde{\Delta}_f^{\text{NL}} = 1.117(7)$ for $\tilde{\kappa}_c = 1.66(1)$ (Fig. 3d).

For intermediate values of ϕ , including $\phi = \pi/2$, $\tilde{\Delta}_f$ and $\tilde{\Delta}_\kappa$ must be simultaneously swept along a hyperbolic trajectory defined by $\tilde{\Delta}_\kappa \tilde{\Delta}_f = 2 \sin(\phi)$ ($\tilde{q} = 0$ in Eq. 11). This trajectory crosses both the EP and the TPD, and is achieved using a parameter control system (Methods), with $(\tilde{\Delta}_\kappa^{\text{EP}}, \tilde{\Delta}_f^{\text{EP}}) = (\pm\sqrt{2}, \pm\sqrt{2})$. Experimentally, we calibrate $\phi = \pi/2$, $J = 0.95$ MHz, and $\tilde{\Delta}_\kappa$ is chosen as the independent variable, with the control system automatically adjusting $\tilde{\Delta}_f$ at each step to stay on the hyperbolic trajectory. Figure 3e-f depicts the EP at $(\tilde{\Delta}_\kappa^{\text{EP}}, \tilde{\Delta}_f^{\text{EP}}) = (-\sqrt{2}, -\sqrt{2})$, projected onto the $\tilde{\Delta}_\kappa$ axis. The TPD locations are found from the roots of a quartic equation, with coefficients dependent on $\phi, \tilde{\kappa}_c$, and cannot be written in closed form (see Supplementary Information for details). Figure 3e depicts the TPD at $(\tilde{\Delta}_\kappa^{\text{TPD}}, \tilde{\Delta}_f^{\text{TPD}}) = (-0.860(3), -2.327(9))$ for $\tilde{\kappa}_c = 1.30(1)$, Fig. 3f has $(\tilde{\Delta}_\kappa^{\text{TPD}}, \tilde{\Delta}_f^{\text{TPD}}) = (-0.657(4), -3.04(2))$ for $\tilde{\kappa}_c = 2.32(3)$ (both projected onto the $\tilde{\Delta}_\kappa$ axis). As shown in Fig. 2c.iii-iv, the instability transition does not occur within a meaningful operating regime for the $\phi = \pi/2$ primary configuration.

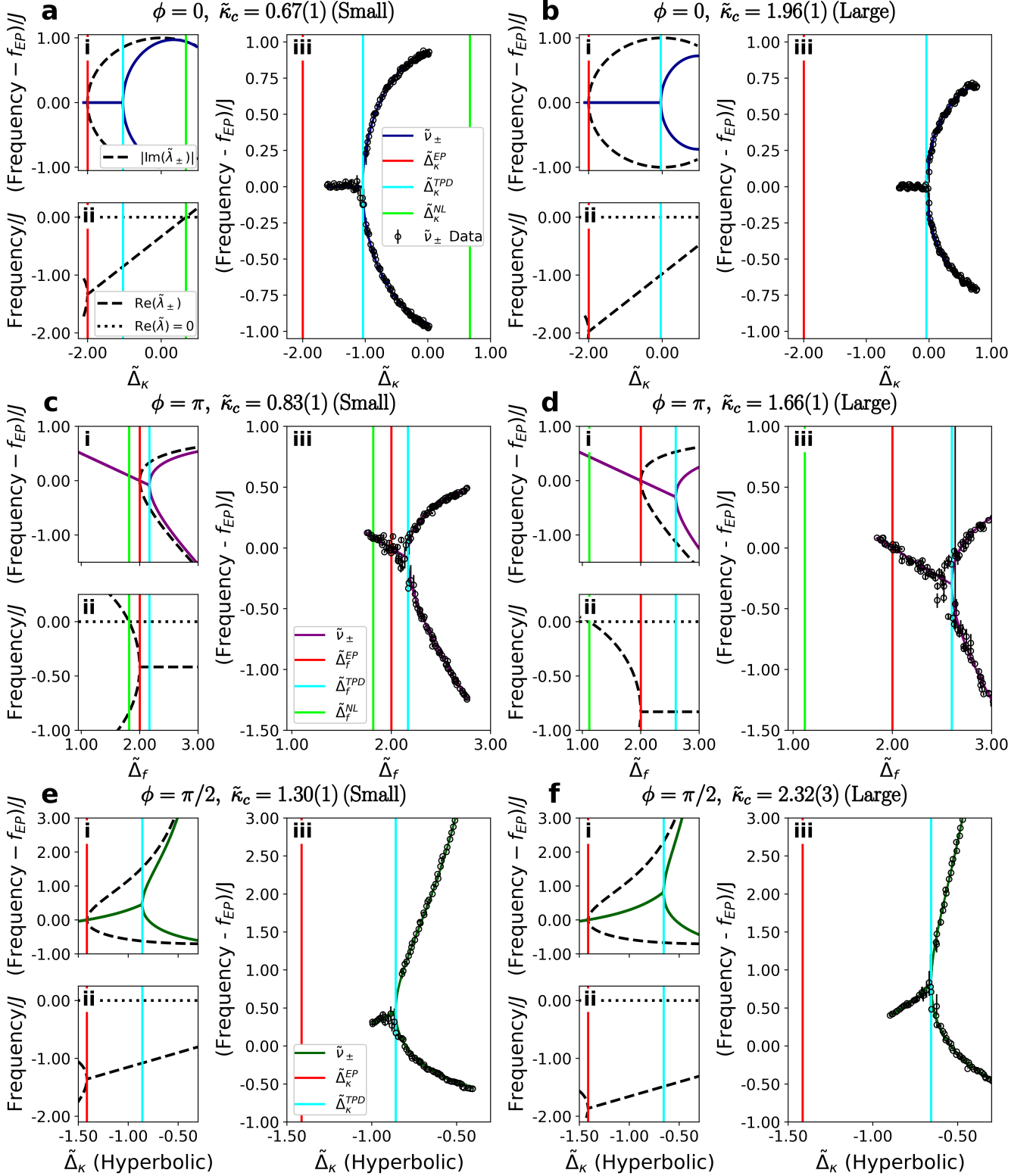


Figure 3. **Surveying a Surface of EPs and TPDs.** Representative EP and TPDs for various ϕ and $\tilde{\kappa}_c$. **i** depicts imaginary eigenvalue splitting at the EPs, and transmission peak splitting at the TPDs for $\phi = 0$ (**a-b**), $\phi = \pi$ (**c-d**) and $\phi = \pi/2$ (**e-f**). The TPD moves with $\tilde{\kappa}_c$, with the left (right) column surveying smaller (larger) $\tilde{\kappa}_c$ values that place the TPD and EP closer to (further from) each other. **ii** depicts real eigenvalues, which also split at EPs, and cross 0 at an instability transition. **iii** Experimentally measured transmission peak locations overlaid atop theory, with error bars representing fit uncertainty propagated from $\sigma(\tilde{\Delta}_f), \sigma(\tilde{\Delta}_\kappa)$ (Methods). Error bars are scaled by 5 to improve visibility, most error bars are contained within the data points.

A. Figures of Merit of Transmission Peak Degeneracies

A critical implication of separating EPs and TPDs is that TPDs can be moved around in parameter space using $\tilde{\kappa}_c$, without changing the location of EPs. We have shown in Fig. 2iii-iv that the proximity of TPDs to EPs changes the Petermann noise factor at the TPD. This relationship is illustrated for a range of $\tilde{\kappa}_c$ values in Fig. 4iv-v, with Fig. 4iv depicting the euclidean distance in the $\tilde{\Delta}_\kappa$ - $\tilde{\Delta}_f$ plane between the primary TPD and the nearest EP, and Fig. 4v depicting the Petermann noise factor at the TPD. Circles (triangles) in Fig. 4b represent $\tilde{\kappa}_c$ values chosen for Fig. 3a,c,e(b,d,f). At $\phi = 0, \tilde{\kappa}_c = 2$, a TPD occurs with minimal \tilde{K}_2 and thus an orthogonal eigenbasis. Here we report other useful figures of merit for TPDs, and show that while \tilde{K}_2 can be reduced by shifting a TPD away from the EP, other relevant characteristics that depend on ϕ and $\tilde{\kappa}_c$ can be used to describe the performance of TPDs.

The concept of splitting strength was initially introduced for EP-based sensors in Ref. [51] to quantify the pre-factor of the square root splitting with respect to the perturbation being measured. Specifically, near an EP, the splitting of imaginary eigenvalues follows $|\text{Im}(\tilde{\Delta}_\lambda)| \approx 2\sqrt{\tilde{\epsilon}}$, where $\tilde{\epsilon} = \epsilon/J$ for a perturbation ϵ in either $\tilde{\Delta}_\kappa$ or $\tilde{\Delta}_f$. For $\phi = \pi/2$, the EP strength is still 2 as long as $\tilde{\epsilon}$ is a perturbation along the hyperbolic trajectory $\tilde{q} = 0$. Recent work has reported the splitting strength of the $\phi = \pi$ TPD [5]. Here, we extend this concept to all TPDs by analyzing the Puiseux series expansion of $\tilde{\Delta}_\nu$ around the TPD, with respect to $\tilde{\epsilon}$, and find

$$\tilde{\Delta}_\nu^{\phi=0}(\tilde{\epsilon}(\tilde{\Delta}_\kappa)) \approx \sqrt{2} (8 - \tilde{\kappa}_c^2)^{1/4} \sqrt{\tilde{\epsilon}(\tilde{\Delta}_\kappa)}, \quad (14)$$

$$\tilde{\Delta}_\nu^{\phi=\pi}(\tilde{\epsilon}(\tilde{\Delta}_f)) \approx \underbrace{\sqrt{2} (\tilde{\kappa}_c^2 + 4)^{1/4}}_{\text{strength coefficient, } \tilde{a}} \sqrt{\tilde{\epsilon}(\tilde{\Delta}_f)}. \quad (15)$$

For $\phi = \pi/2$, the strength cannot be written in closed form, but is plotted in Fig. 4b.ii along with Eq. 14 and Eq. 15. We stress that for the $\phi = \pi/2$ TPD, the strength coefficient is normalized based on a perturbation exactly along the hyperbolic path $\tilde{q} = 0$. If strength is projected onto either the $\tilde{\Delta}_\kappa$ or $\tilde{\Delta}_f$ axis, the splitting is significantly stronger than for the $\phi = 0, \pi$ TPD.

Parameter hypersensitivity exists as a challenge for EPs and was recently explored for the $\phi = 0$ TPD [19]. Here, we report one quantitative measure of the effect of hypersensitivity on TPDs. The split peaks of the experimental data in Fig. 4a have an abrupt jump near the TPD, indicating that $\tilde{\Delta}_\nu$ fails to smoothly approach zero at the TPD itself. If the TPD is crossed with a path in parameter space where $\tilde{q} \neq 0$, due to fabrication or operational errors, peak splitting will still occur, but not with a continuous square root profile. Instead, the splitting is zero until it jumps to $\min(\tilde{\Delta}_\nu) \neq 0$, increasing from there. Mathematically, we find that the minimum

splitting can be expressed in terms of \tilde{q} as

$$\min(\tilde{\Delta}_\nu) = \frac{3}{2^{1/3}} |\tilde{q}|^{1/3}, \quad (16)$$

with a derivation involving the geometry of the roots of Eq. 9 in the Supplementary Information. $\min(\tilde{\Delta}_\nu) = \tilde{a}\sqrt{\tilde{\epsilon}_{\min}}$ bounds the minimum perturbation that can be resolved, limiting the precision of the TPD. The exact value of $\min(\tilde{\Delta}_\nu)$ is based on how far off the $\tilde{q} = 0$ path an experiment strays. For the $\phi = 0$ ($\phi = \pi$) TPD, this occurs when $\tilde{\Delta}_f \neq 0$ ($\tilde{\Delta}_\kappa \neq 0$). Our calculations use the convergence threshold of the control system to calculate the maximum \tilde{q} deviation (Methods). $\min(\tilde{\Delta}_\nu)$ is plotted in Fig. 4b.iii, illustrating its dependence on ϕ and $\tilde{\kappa}_c$.

The promise of EP-based sensors revolves around the potential to attain an infinite derivative response exactly at the onset of square root splitting. For TPDs, splitting strength and minimum splitting combine into a more realistic picture for the maximum possible derivative. Around the TPD, $\tilde{\Delta}_\nu \approx \tilde{a}\sqrt{\tilde{\epsilon}}$, where \tilde{a} is the normalized strength of the TPD, with derivative $\tilde{a}/2\sqrt{\tilde{\epsilon}}$. The maximum value of this derivative is based on the minimum resolvable $\tilde{\epsilon}$, with Max Derivative = $\tilde{a}^2/(2\min(\tilde{\Delta}_\nu))$ plotted in Fig. 4b.i.

The figures of merit introduced in this section can be used as a guide to optimize TPD-based sensors. For example, the $\phi = 0$ TPD should be used with $\tilde{\kappa}_c = 2$, minimizing \tilde{K}_2 and $\min(\tilde{\Delta}_\nu)$ at the cost of some splitting strength. For the $\phi = \pi$ TPD, response can be maximized by moving the TPD closer to the EP, which inadvertently drastically increases the Petermann noise factor. Ultimately, the design of TPD-based sensors must balance competing metrics based on the constraints and goals of the specific experimental platform.

IV. CONCLUSION AND OUTLOOK

This work presents a highly tunable experimental platform and a unified theoretical framework for systematically investigating EPs and TPDs in coupled oscillator systems. A synthetic gauge field is engineered through the complex coupling term $Je^{i\phi}$, effectively unifying previously distinct two-dimensional configurations of EPs and TPDs into a surface of EPs and TPDs. We report the distinct properties of the EPs and TPDs at $\phi = 0, \pi$, and $\pi/2$, with analysis and methods that can be extended to any value of ϕ . Our magnon-photon platform offers practical pathways towards implementing new TPD-based sensors. Specifically, by including the magnon mode, our system allows for direct observation of external magnetic fields through the frequency detuning Δ_f in the $\phi = \pi$ configuration, or external electric fields that modify the analog attenuator, adjusting κ_y and thus dissipation detuning Δ_κ in the $\phi = 0$ configuration. Furthermore, sensors that utilize passive or active feedback systems to remain on the hyperbolic trajectory around the TPDs described for other values of ϕ

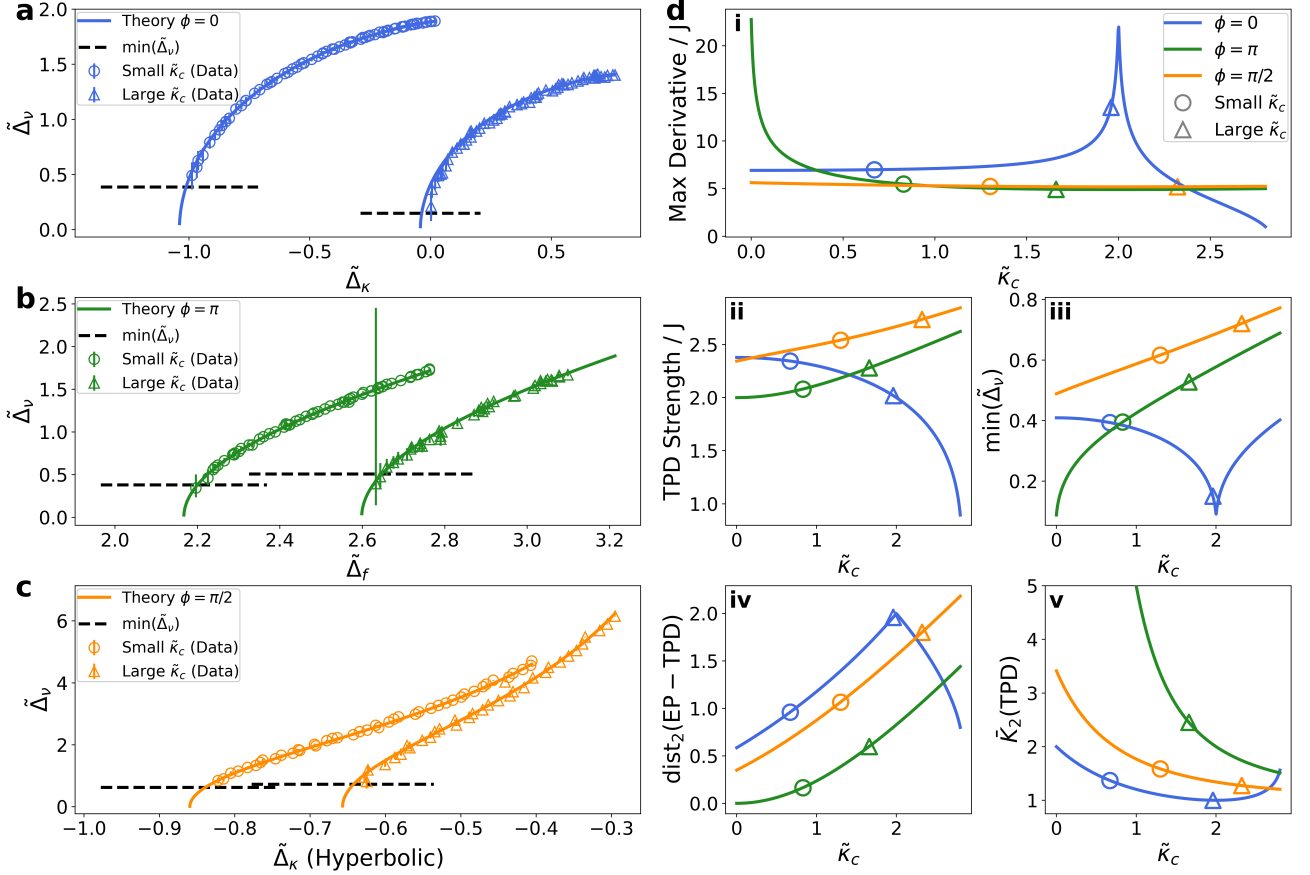


Figure 4. **Figures of Merit for TPDs.** **a-c**, Experimental data from Fig. 3iii, recast as $\tilde{\Delta}_\nu = \tilde{\nu}_+ - \tilde{\nu}_-$ for representative small $\tilde{\kappa}_c$ (circle) and large $\tilde{\kappa}_c$ (triangle) directly compared at $\phi = 0$ (**a**), $\phi = \pi$ (**b**), $\phi = \pi/2$ (**c**). Horizontal lines depict theoretical $\min(\tilde{\Delta}_\nu)$ quantified using uncertainties in the experimental apparatus. Data illustrate that the pre-factor of the square root splitting, as well as the minimum resolvable splitting, depend on $\tilde{\kappa}_c$. **d** depicts figures of merit for TPDs, including **i** maximum derivative, **ii** TPD splitting strength, **iii** minimum resolvable splitting, **iv**, euclidean distance from TPD to nearest EP, and **v** Petermann noise factor (\tilde{K}_2) at the TPD.

could be used to further enhance sensor response. In this work, we focus on demonstrating the broad tunability of our architecture, but future research can leverage this platform to engineer robust and optimized sensors that likely have less tunability to avoid parameter hypersensitivity issues.

The framework and methods developed in this study may extend beyond semi-classical dimers. For example, our system naturally lends itself to the study of nonlinear phenomena associated with EPs and TPDs, due to the active gain elements that saturate in the unstable regime [35]. The mathematical tools and experimental methods demonstrated here may be generalized to higher-dimensional lattices and more complex resonators and oscillator networks, potentially revealing new spectral phenomena, topological behaviors, higher-dimensional exceptional surfaces, and higher order EPs [20], or even higher-order TPDs. We leave these exciting steps to future work.

V. METHODS

A. Device Description

Our setup includes a vector network analyzer (Quantum Machines OPX+ Quantum Controller) and a local oscillator (SignalCore SC5511A) for collecting the data displayed in Fig. 1, 3, 4. Our apparatus consists of a custom-built microwave cavity with mechanically tunable frequency and output-port coupling rates and a custom-built oscillator realized from a 1 mm diameter YIG sphere, placed on top of a co-planar waveguide (Minicircuits CMA-83LN+). The YIG sphere is coupled to the ground using orthogonal wire bonds. Magnon and photon modes are coupled over a meter-scale distance using flexible SMA wires (Minicircuits 086-11SM+). To achieve variable gain amplification and tunable coupling, we place a fixed-gain amplifier (Minicircuits CMA-83LN+), directly followed by a digital attenuator (Vaunix LDA-5018V), and tune the attenuation

digitally using the Vaunix Python API. A digital phase shifter (Vaunix LPS-802) modifies the phase for hopping between the cavity and YIG.

We use three digital switches to probe each mode individually during experimental operation without modifying the apparatus. Two Vaunix LSW-802P4T switches (1-input, 4-output) are used on the drive and readout lines to select which mode is being driven or read out. A 1-input, 2-output (Vaunix LSW-802PDT) switch is included on one of the coupling wires to disable or enable coupling when probing each mode individually. When disabled, the signal is routed directly to a 50- Ω terminator to ensure impedance matching and reduce reflections. Furthermore, when coupling is disabled, all digital attenuators are set to their maximum attenuation (50 dB) to provide additional isolation. Directional couplers (Minicircuits ZADC-13-73-S+) drive and read out each mode, attaching to the self-feedback loops.

Experimental control of parameters is achieved through a Python API. f_y is primarily tuned using an external magnetic field controlled by an electromagnet driven by a digital current source (SRS CS580). We offset the frequency of the YIG to 6 GHz using a fixed neodymium magnet and finely tune B_z using the current source. To modify κ_y with high resolution, we insert an analog voltage-controlled attenuator (Analog Devices HMC812ALC4 integrated with EV1 eval board) on the YIG self-feedback loop, and modify the voltage using precision voltage source (SRS DC205). A full schematic diagram including all components and wiring is included in the Supplementary Information.

B. Parameter Calibration

During an experimental sweep, all the parameters $f_c, f_y, \kappa_c, \kappa_y, J, \phi$ are necessary for data analysis. Parameters $f_c, f_y, \kappa_c, \kappa_y$ are measured during each step of the independent variable, using the RF-switch-based probing method described in Sec. V A. To determine ϕ , we use the experimental apparatus to set $f_c = f_y$ and $\kappa_c = \kappa_y$, then couple the two modes together and change the digital phase shifter until the hybridized peaks are the same height in transmission, which defines the phase origin, $\phi = 0$. Finally, J is a fitted parameter, extracted once for each value of loop attenuation and loop phase.

C. Experimental Non-idealities

Although the experimental platform enables precise control over key parameters, residual experimental uncertainties persist. For instance, we have observed that modifications of phases can result in changes to effective loss rates due to interference, effectively creating crosstalk between experimental parameters for each mode. However, since we can separately infer $f_c, f_y, \kappa_c, \kappa_y$, we can calibrate away any crosstalk between

these variables in our system. However, experimental nonidealities cannot be ignored for the RP-TPD experimental sweep, where the voltage-controlled attenuator described in Sec. V A is swept. The voltage-controlled attenuator imparts a significant phase shift while modifying attenuation. This parasitic phase shift causes the YIG frequency f_y to drastically change during the RPEP experimental sweep, deviating from the required $\Delta_f = 0$ path needed to see the RP-TPD. To account for this, we implement a simple digital proportional feedback control system with the current-controlled electromagnet to correct f_y and keep $\Delta_f = 0$ while changing Δ_κ . The effect of this control system is included in the Supplementary Information. Additionally, for the RP configuration, the maximum κ_y is limited to ~ 5 MHz before the YIG resonance is indistinguishable from the system noise floor. Thus, this limits the choices of J and κ_c for experimental scans to ensure that κ_y does not breach this maximum threshold before the TPD is reached.

D. Parameter Control System

Due to the non-idealities described in Sec. V C, we model the relationship between coil current (I), attenuator voltage (V), and the measured parameters (f_y, κ_y) using regression. The pair (I, V) are swept over a dense grid of $N = 1200$ points. At each (I, V) we measure (f_y, κ_y) via a Lorentzian fit of transmission. To capture the weak nonlinearities of the voltage-controlled attenuator we use the feature vector $\psi(I, V) = [I, V, IV, V^2, 1, V]^T$ and perform least-squares regression using NumPy to obtain a weight matrix $\Theta \in \mathbb{R}^{6 \times 2}$ which maps features to predicted outputs as

$$\begin{bmatrix} \hat{f}_y \\ \hat{\kappa}_y \end{bmatrix} = \Theta^T \cdot \psi(I, V). \quad (17)$$

The model achieves $R^2 \approx 0.995$ for both I and V and RMSE on the order of ≈ 10 KHz.

During an experimental sweep, this model serves as a feedforward map from control inputs (I, V) to predicted outputs ($\hat{f}_y, \hat{\kappa}_y$). The inverse problem is solved via Newton's method to find the input required to attain a specified target. At each iteration, a new measurement of (f_y, κ_y) is taken. Every 5 iterations, a new measurement of (f_c, κ_c) is taken to account for noise in the cavity. We calculate $(\Delta_f, \Delta_\kappa)$ and the absolute error relative to the target $(\Delta_f^{\text{Target}}, \Delta_\kappa^{\text{Target}})$ is computed, and a Jacobian is constructed analytically from the regression model. A damped Newton update with gain matrix $K_p = \text{diag}([0.8, 0.8])$ is applied to (I, V), and the process repeats until the error is within a specified tolerance, $\Delta_f^{\text{err}}, \Delta_\kappa^{\text{err}} = [10^{-5}, 10^{-5}]$. This protocol enables tracking of arbitrary paths in $(\Delta_f, \Delta_\kappa)$ using only a learned model and analytical Jacobian.

E. Data Analysis

In the Main Text, we strictly use nondimensionalized parameters to present the data. However, when performing data analysis, we use the dimensional parameters, and scale by J at the end. When probing the YIG or cavity individually using the RF-switch-based isolation method, we convert the output data extracted from the OPX+ Quantum Controller into a linear scale and fit the data to a Lorentzian profile. From the fit, we extract $f_c, f_y, \kappa_c, \kappa_y$, and $\sigma(f_c), \sigma(f_y), \sigma(\kappa_c), \sigma(\kappa_y)$ using the elements of the least squares regression covariance matrix. Then, for data where the coupling is enabled, we fit ν_{\pm} to the data using $f_c, f_y, \kappa_c, \kappa_y$, and J , which is determined from Sec. VB which we scale by J and report as experimental data in Fig. 3 as $\tilde{\nu}_{\pm}$. To quantify the fit uncertainty of ν_{\pm} , we fit the data $N = 10^4$ times drawing from a multivariate normal distribution in $f_c, f_y, \kappa_c, \kappa_y$ with uncertainties $\sigma(f_c), \sigma(f_y), \sigma(\kappa_c), \sigma(\kappa_y)$. For each shot in N , we calculate ν_{\pm} , yielding a distribution $\mathcal{D}(\nu_{\pm})$ with standard deviation $\sigma(\nu_{\pm})$. The error bars in Fig. 3 are $\sigma(\nu_{\pm})/J$, a measure of the propagation of uncertainty of the fit parameters to the peak locations of the coupled system.

We also seek to obtain a measure of global uncertainty across the entire experiment, accounting for variations in κ_c across an entire sweep. The average κ_c is reported as data (in the form $\tilde{\kappa}_c$, with experimental uncertainty

$\sigma_{\text{exp}}(\tilde{\kappa}_c)$ equal to the standard deviation of κ_c across the sweep. The location of EPs, TPDs, and instability transitions are calculated using J, κ_c . $\sigma_{\text{exp}}(\kappa_c)$ propagates to the location of EPs, TPDs, and instability, which we report in Sec. III. For $\phi = 0$ and $\phi = \pi$, a closed form solution for the propagation of uncertainty from $\tilde{\kappa}_c$ exists. For other values of ϕ , which require finding roots of a quartic, a Monte Carlo propagation of uncertainty technique is used instead. The resulting error propagation is relatively small, so we choose to omit it from Fig. 3.

Beyond the instability transition, the linear model is no longer valid, and the experimental results are no longer well-described by T_{Coupled} . We hope to explore the complete nonlinear model that considers amplifier saturation and other nonlinear stabilization effects in future work.

VI. DATA AVAILABILITY

The data that support the findings of this study are available upon reasonable request.

VII. CODE AVAILABILITY

The data analysis code will be available online on GitHub.

-
- [1] J. Wiersig, *Photonics Research* **8**, 1457 (2020).
 - [2] J. Wiersig, *Physical Review A* **93**, 033809 (2016), publisher: American Physical Society.
 - [3] J. Wiersig, *Physical Review Letters* **112**, 203901 (2014), publisher: American Physical Society.
 - [4] J.-H. Park, A. Ndao, W. Cai, L. Hsu, A. Kodigala, T. Lepetit, Y.-H. Lo, and B. Kanté, *Nature Physics* **16**, 462 (2020), publisher: Nature Publishing Group.
 - [5] R. Kononchuk, J. Cai, F. Ellis, R. Thevamaran, and T. Kottos, *Nature* **607**, 697 (2022), publisher: Nature Publishing Group.
 - [6] A. Suntharalingam, L. Fernández-Alcázar, R. Kononchuk, and T. Kottos, *Nature Communications* **14**, 5515 (2023), publisher: Nature Publishing Group.
 - [7] W. D. Heiss, *Journal of Physics A: Mathematical and Theoretical* **45**, 444016 (2012), publisher: IOP Publishing.
 - [8] W. Chen, Ş. Kaya Ozdemir, G. Zhao, J. Wiersig, and L. Yang, *Nature* **548**, 192 (2017).
 - [9] H. Wang, Y.-H. Lai, Z. Yuan, M.-G. Suh, and K. Vahala, *Nature Communications* **11**, 1610 (2020), publisher: Nature Publishing Group.
 - [10] A. E. Siegman, *Physical Review A* **39**, 1264 (1989), publisher: American Physical Society.
 - [11] W. Langbein, *Physical Review A* **98**, 023805 (2018), arXiv:1801.05750 [physics].
 - [12] S. Soleymani, Q. Zhong, M. Mokim, S. Rotter, R. El-Ganainy, and S. K. Ozdemir, *Nature Communications* **13**, 599 (2022).
 - [13] N. A. Mortensen, P. a. D. Gonçalves, M. Khajavikhan, D. N. Christodoulides, C. Tserkezis, and C. Wolff, *Optica* **5**, 1342 (2018), publisher: Optica Publishing Group.
 - [14] J. Wiersig, *Nature Communications* **11**, 2454 (2020), publisher: Nature Publishing Group.
 - [15] M. J. Grant and M. J. F. Digonnet, *Optics Letters* **46**, 2936 (2021), publisher: Optica Publishing Group.
 - [16] H. Loughlin and V. Sudhir, *Physical Review Letters* **132**, 243601 (2024).
 - [17] M. Zhang, W. Sweeney, C. W. Hsu, L. Yang, A. D. Stone, and L. Jiang, *Physical Review Letters* **123**, 180501 (2019), publisher: American Physical Society.
 - [18] Q. Geng and K.-D. Zhu, *Photonics Research* **9**, 1645 (2021), publisher: Optica Publishing Group.
 - [19] X. Lu, Y. Yuan, F. Chen, X. Hou, Y. Guo, L. Reindl, Y. Fu, W. Luo, and D. Zhao, *Microsystems & Nano-engineering* **11**, 1 (2025), publisher: Nature Publishing Group.
 - [20] H. Hodaie, A. U. Hassan, S. Wittek, H. Garcia-Gracia, R. El-Ganainy, D. N. Christodoulides, and M. Khajavikhan, *Nature* **548**, 187 (2017), publisher: Nature Publishing Group.
 - [21] W. Chen, J. Zhang, B. Peng, S. K. Ozdemir, X. Fan, and L. Yang, *Photonics Research* **6**, A23 (2018), publisher: Optica Publishing Group.

- [22] M. Brandstetter, M. Liertzer, C. Deutsch, P. Klang, J. Schöberl, H. E. Türeci, G. Strasser, K. Unterrainer, and S. Rotter, *Nature Communications* **5**, 4034 (2014), publisher: Nature Publishing Group.
- [23] Z. Dong, Z. Li, F. Yang, C.-W. Qiu, and J. S. Ho, *Nature Electronics* **2**, 335 (2019), publisher: Nature Publishing Group.
- [24] J. D. Huerta-Morales, M. A. Quiroz-Juárez, Y. N. Joglekar, and R. d. J. León-Montiel, *Physical Review A* **107**, 042219 (2023), publisher: American Physical Society.
- [25] M. Naghiloo, M. Abbasi, Y. N. Joglekar, and K. W. Murch, *Nature Physics* **15**, 1232 (2019), publisher: Nature Publishing Group.
- [26] W. Chen, M. Abbasi, B. Ha, S. Erdamar, Y. N. Joglekar, and K. W. Murch, *Physical Review Letters* **128**, 110402 (2022), publisher: American Physical Society.
- [27] D. Zhang, X.-Q. Luo, Y.-P. Wang, T.-F. Li, and J. Q. You, *Nature Communications* **8**, 1368 (2017), publisher: Nature Publishing Group.
- [28] G.-Q. Zhang and J. Q. You, *Physical Review B* **99**, 054404 (2019), publisher: American Physical Society.
- [29] B. Zare Rameshti, S. Viola Kusminskiy, J. A. Haigh, K. Usami, D. Lachance-Quirion, Y. Nakamura, C.-M. Hu, H. X. Tang, G. E. W. Bauer, and Y. M. Blanter, *Physics Reports Cavity Magnonics*, **979**, 1 (2022).
- [30] M. Harder, Y. Yang, B. Yao, C. Yu, J. Rao, Y. Gui, R. Stamps, and C.-M. Hu, *Physical Review Letters* **121**, 137203 (2018).
- [31] C. Owens, A. LaChapelle, B. Saxberg, B. M. Anderson, R. Ma, J. Simon, and D. I. Schuster, *Physical Review A* **97**, 013818 (2018), publisher: American Physical Society.
- [32] B. Yao, T. Yu, X. Zhang, W. Lu, Y. Gui, C.-M. Hu, and Y. M. Blanter, *Physical Review B* **100**, 214426 (2019), publisher: American Physical Society.
- [33] A. Gardin, G. Bourcin, J. Bourhill, V. Vlamincq, C. Person, C. Fumeaux, G. C. Tettamanzi, and V. Castel, *Physical Review Applied* **21**, 064033 (2024), publisher: American Physical Society.
- [34] Y.-P. Wang and C.-M. Hu, *Journal of Applied Physics* **127**, 130901 (2020).
- [35] J. S. Salcedo-Gallo, M. Burgelman, V. P. Flynn, A. S. Carney, M. Hamdan, T. Gerg, D. C. Smallwood, L. Viola, and M. Fitzpatrick, *Demonstration of a tunable non-hermitian nonlinear microwave dimer* (2025), arXiv:2503.13364 [quant-ph].
- [36] Z. Pang, B. T. T. Wong, J. Hu, and Y. Yang, *Physical Review Letters* **132**, 043804 (2024), publisher: American Physical Society.
- [37] N. Hatano and D. R. Nelson, *Physical Review Letters* **77**, 570 (1996), publisher: American Physical Society.
- [38] R. Wen, C.-L. Zou, X. Zhu, P. Chen, Z. Ou, J. Chen, and W. Zhang, *Physical Review Letters* **122**, 253602 (2019), publisher: American Physical Society.
- [39] M. Reagor, W. Pfaff, C. Axline, R. W. Heeres, N. Ofek, K. Sliwa, E. Holland, C. Wang, J. Blumoff, K. Chou, M. J. Hatridge, L. Frunzio, M. H. Devoret, L. Jiang, and R. J. Schoelkopf, *Physical Review B* **94**, 014506 (2016), publisher: American Physical Society.
- [40] M. Sparks, R. Loudon, and C. Kittel, *Physical Review* **122**, 791 (1961), publisher: American Physical Society.
- [41] R. L. Comstock, *Solid State Electronics* **6**, 392 (1963), aDS Bibcode: 1963SSEle...6..392C.
- [42] J. F. Barry, R. A. Irion, M. H. Steinecker, D. K. Freeman, J. J. Kedziora, R. G. Wilcox, and D. A. Braje, *Physical Review Applied* **19**, 044044 (2023).
- [43] J. Rao, C. Wang, B. Yao, Z. Chen, K. Zhao, and W. Lu, *Physical Review Letters* **131**, 106702 (2023), publisher: American Physical Society.
- [44] M. C. Zheng, D. N. Christodoulides, R. Fleischmann, and T. Kottos, *Physical Review A* **82**, 010103 (2010), publisher: American Physical Society.
- [45] Y. Ashida, Z. Gong, and M. Ueda, *Advances in Physics* **69**, 249 (2020), arXiv:2006.01837 [cond-mat].
- [46] H. Zhou, J. Y. Lee, S. Liu, and B. Zhen, *Optica* **6**, 190 (2019), publisher: Optica Publishing Group.
- [47] S. Ghosh, A. Roy, S. Dey, B. P. Pal, and S. Ghosh, *JOSA B* **41**, 2534 (2024), publisher: Optica Publishing Group.
- [48] R. W. D. Nickalls, *The Mathematical Gazette* **90**, 203 (2006).
- [49] G. C. Holmes, *The Mathematical Gazette* **86**, 473 (2002).
- [50] F. Viète, *Opera mathematica* **volume 4** (1615).
- [51] J. Wiersig, in *Parity-time Symmetry and Its Applications*, edited by D. Christodoulides and J. Yang (Springer, Singapore, 2018) pp. 155–184.

ACKNOWLEDGMENTS

We thank Joe Poissant for his exceptional support in designing and fabricating the 3D microwave cavities. We thank Lorenza Viola, Michiel Burgelman, and Vincent P. Flynn for their contributions to the foundational work upon which this study builds and for valuable discussions about EPs. We thank Hailey A. Mullen, Tian Xia, and Sam Sacerdote for valuable discussions and feedback on the manuscript. We also thank Dr. Mukund Vengalattore for the valuable guidance and support of the project. Startup funds from the Thayer School of Engineering, Dartmouth College, supported this work. We gratefully acknowledge support from the DARPA Young Faculty Award No. D23AP00192, and from the NSF through Grant DGE-2125733. The views and conclusions in this manuscript are those of the authors. They should not be interpreted as representing the official policies, expressed or implied, of DARPA, NSF, or the US Government. The US Government is authorized to reproduce and distribute reprints for Government purposes, notwithstanding any copyright notation herein.

VIII. AUTHOR CONTRIBUTIONS

A.S.C., J.S.S.G., and M.F. conceived and designed the experiments, while A.S.C. performed the final set of experiments and calibrations. The theoretical model was conceived by A.S.C. and M.F., and formalized and presented by A.S.C., with S.B. developing and presenting the motivation and derivation of the dynamical matrix. A.S.C. conceived of the reported TPD figures of merit, as well as non-reciprocal-phase TPDs and the experimental control methods necessary to observe them. A.S.C.

collected, managed, and analyzed data, while generating numerical and analytical simulations, receiving feedback from M.F. All authors jointly validated the results. A.S.C. wrote the manuscript, with copious edits and suggestions from M.F. and edits from J.S.S.G. S.B provided edits and contributed to the introduction, literature review, and supplementary information. M.F. conceived of and supervised the project.

IX. COMPETING INTERESTS

The authors declare no competing interests.

X. ADDITIONAL INFORMATION

A. Supplementary Information

In this preprint version, the Main Manuscript and Supplementary Information are provided as a single file for immediate access.

B. Correspondence and Request for Materials

Correspondence and material requests should be directed to Mattias Fitzpatrick (mattias.w.fitzpatrick@dartmouth.edu) and Alexander S. Carney (alexander.s.carney.th@dartmouth.edu), respectively. Data supporting the findings of this study are available from the corresponding author upon reasonable request.

Supplementary Information: Unification of Exceptional Points and Transmission Peak Degeneracies in a Highly Tunable Magnon-Photon Dimer

Alexander S. Carney,¹ Juan S. Salcedo-Gallo,¹ Salil K. Bedkihal,¹ and Mattias Fitzpatrick^{1,2}

¹*Thayer School of Engineering, Dartmouth College, 15 Thayer Drive, Hanover, New Hampshire 03755, USA*

²*Department of Physics and Astronomy, Dartmouth College, 6127 Wilder Laboratory, Hanover, New Hampshire 03755, USA*

This supplementary document offers additional details about the theory used in the Main Text to describe the dynamics of the system. We also additional experimental details outside of what is provided in the Methods section of the Main Text.

CONTENTS

I. Theoretical Model	2
A. Non-reciprocal Dissipative Magnon-Photon Coupling	2
B. Classically coupled oscillators with Broken reciprocity	3
C. Theory for the Linear Model: Equations of Motion	3
D. Petermann Factor Analysis	5
E. Cube Roots and TPDs	6
F. Parameterization of TPD Surface	7
G. Coupled Transmission Equation	7
H. Geometric Interpretation of Peaks and Imaginary Eigenvalues	7
I. Effect of Drive and Readout Vector on Peak Locations	8
II. Experimental Details	8
A. YIG Ferromagnetic Resonance	8
B. Device Schematics	8
References	9

I. THEORETICAL MODEL

A. Non-reciprocal Dissipative Magnon-Photon Coupling

We first present a physical motivation of an effective non-Hermitian Hamiltonian for a coupled magnon-photon dimer. The dynamical matrix used for the analysis resembles that of the dissipative magnon-photon coupling Hamiltonian used in cavity magnonics [1]. Dissipative magnon-photon coupling was initially understood through a phenomenological electrodynamic framework. In this picture, Ampère's law explains how a microwave current \mathbf{j} generates an AC magnetic field that exerts a driving torque on the magnetization of the YIG sample. In return, dynamic magnetization \mathbf{m} influences the RF current via the Faraday effect. This mutual interaction leads to a form of dissipative coupling, effectively captured by a non-Hermitian term in the description of the system. This term models the backaction of the induced RF current on the magnetization dynamics, acting to impede rather than drive the motion. This framework has laid the foundation for understanding phase nonreciprocity and non-Hermitian dynamics in hybrid magnon-photon systems. In this picture, the following Hamiltonian has been proposed to model the dissipative magnon-photon coupling: [2–6]

$$\hat{H} = \omega_1 \hat{a}_1^\dagger \hat{a}_1 + \omega_2 \hat{a}_2^\dagger \hat{a}_2 + J \left(\hat{a}_1^\dagger \hat{a}_2 + e^{i\phi} \hat{a}_2^\dagger \hat{a}_1 \right), \quad (\text{S1})$$

where ω_1 and ω_2 represent cavity and the magnon mode frequencies respectively. Notice that for $\phi = 0$ and $\phi = \pi$ the coupling becomes coherent and for other phases it is both dissipative and coherent. In the subsequent section, we adapt this Hamiltonian and obtain equations of motion in the semiclassical limit. Non-reciprocal hopping in Eq. S1 can emerge due to dissipative effects mediated by a shared environment. It can be thought of as a non-Hermitian beam-splitter. For completeness, we would like to briefly summarize a quantum model and present an argument for phase non-reciprocity so as to motivate the dynamical matrix used in this work. The microscopic derivation of non-reciprocal magnon-photon interactions using traveling wave amplifiers has been presented here [7].

We consider two coupled modes, both coherently and dissipatively through a shared reservoir [8]. The coherent interaction is described by the Hamiltonian

$$\hat{H}_{\text{coh}} = \hbar J \left(\hat{a}^\dagger \hat{b} + \hat{b}^\dagger \hat{a} \right),$$

where J is the coherent coupling strength.

Dissipative coupling is introduced through a shared reservoir, characterized by the jump operator

$$\hat{o} = \hat{a} + r e^{i\theta} \hat{b},$$

where r is a real amplitude ratio and θ is the relative phase. This yields a non-Hermitian contribution to the effective Hamiltonian,

$$\hat{H}_{\text{diss}} = -\frac{i\gamma}{2} \hat{o}^\dagger \hat{o} = -\frac{i\gamma}{2} \left(\hat{a}^\dagger + r e^{-i\theta} \hat{b}^\dagger \right) \left(\hat{a} + r e^{i\theta} \hat{b} \right).$$

Expanding this equation gives the diagonal and the off-diagonal terms, and the dissipative part becomes

$$\hat{H}_{\text{diss}} = -\frac{i\gamma}{2} (a^\dagger a + r^2 b^\dagger b) - \frac{i\gamma r}{2} (e^{i\theta} a b^\dagger + e^{-i\theta} b^\dagger a) \quad (\text{S2})$$

Combining the coherent and dissipative interactions, the off-diagonal part of the Hamiltonian becomes

$$H_o = \left(J - i \frac{\gamma r}{2} e^{-i\theta} \right) a^\dagger b + \left(J - i \frac{\gamma r}{2} e^{i\theta} \right) b^\dagger a \quad (\text{S3})$$

To achieve unidirectional coupling, we set $\theta = \frac{\pi}{2}$, so that $e^{\pm i\theta} = \pm i$, and choose $J = \frac{\gamma r}{2}$. Substituting these values, we find

$$\begin{aligned} \hat{a}^\dagger \hat{b} : \quad & J - i \frac{\gamma r}{2} (-i) = J + \frac{\gamma r}{2} = \gamma r, \\ \hat{b}^\dagger \hat{a} : \quad & J - i \frac{\gamma r}{2} (i) = J - \frac{\gamma r}{2} = 0. \end{aligned}$$

This configuration yields perfect non-reciprocity: excitations transfer from mode a to mode b , but not in the reverse direction.

In the general case, tuning the amplitude r and phase θ of the dissipative off-diagonal coupling suggests the following form of an effective non-Hermitian Hamiltonian

$$\hat{H}_{\text{eff}} = \begin{pmatrix} \omega_a - i\kappa_a & J \\ J e^{i\phi} & \omega_b - i\kappa_b \end{pmatrix},$$

where J is real, and the complex phase ϕ introduces directional asymmetry between the two modes and $\kappa_a = \frac{\gamma}{2}$ and $\kappa_b = \frac{\gamma r^2}{2}$. This structure forms the basis for engineering nonreciprocal dynamics in open quantum systems. In the semi-classical limit it can be thought of as a dynamical non-Hermitian matrix realized in our room temperature set-up. This essentially describes coupled oscillators with broken reciprocity.

B. Classically coupled oscillators with Broken reciprocity

The form of the dynamical matrix used in this work can also be obtained purely from a classical model of interacting harmonic oscillators with broken time reversal symmetry. We consider two coupled classical oscillators $x_1(t)$ and $x_2(t)$ with damping and a non-reciprocal phase in the coupling. The equations of motion are:

$$\ddot{x}_1 + \gamma_1 \dot{x}_1 + \omega_1^2 x_1 + J^2 x_2 = 0, \quad (\text{S4})$$

$$\ddot{x}_2 + \gamma_2 \dot{x}_2 + \omega_2^2 x_2 + J^2 e^{i\phi} x_1 = 0, \quad (\text{S5})$$

where

- ω_1, ω_2 are the natural frequencies of the oscillators,
- γ_1, γ_2 are the damping coefficients,
- K is the real-valued coupling strength,
- ϕ is a non-reciprocal phase (appearing only in one direction of coupling).

This can be written in matrix form as follows. Define $\mathbf{x}(t) = \begin{pmatrix} x_1(t) \\ x_2(t) \end{pmatrix}$, then the equations of motion can be written as:

$$\ddot{\mathbf{x}} + \Gamma \dot{\mathbf{x}} + D \mathbf{x} = 0, \quad (\text{S6})$$

where

$$\Gamma = \begin{pmatrix} \gamma_1 & 0 \\ 0 & \gamma_2 \end{pmatrix}, \quad D = \begin{pmatrix} \omega_1^2 & J^2 \\ J^2 e^{i\phi} & \omega_2^2 \end{pmatrix}.$$

A similar model has been used in the context of dissipative magnon-photon interaction within the radiation damping picture [9, 10]

C. Theory for the Linear Model: Equations of Motion

The equations of motion presented in the draft can be interpreted as the semiclassical limit of an effective non-Hermitian Hamiltonian. This effective Hamiltonian incorporates diagonal self-energy terms to model losses, while the off-diagonal self-energy terms arise from dissipative, phase-dependent hopping. More importantly, the off-diagonal terms can have a nonreciprocal nature. Such a dissipative coupling can be engineered using structured reservoirs such as waveguides and by introducing synthetic gauge fields. We consider a system of coupled oscillators. The effective Hamiltonian for this system in the rotating frame (rotating with drive frequency) can be written as ($\hbar = 1$):

$$\begin{aligned} H_{\text{eff}} = & (\omega_c - \omega_d) a_c^\dagger a_c + (\omega_y - \omega_d) a_y^\dagger a_y \\ & - i \frac{\kappa_c}{2} a_c^\dagger a_c - i \frac{\kappa_y}{2} a_y^\dagger a_y \\ & + J (a_c^\dagger a_y + e^{-i\phi} a_y^\dagger a_c) \\ & + f_c (a_c^\dagger + a_c) + f_y (a_y^\dagger + a_y) \end{aligned} \quad (\text{S7})$$

We consider two non-interacting cavities given by the following Hamiltonian:

$$H_0 = (\omega_c - \omega_d) a_c^\dagger a_c + (\omega_y - \omega_d) a_y^\dagger a_y + u_c (a_c^\dagger + a_c) + u_y (a_y^\dagger + a_y) \quad (\text{S8})$$

The effective non-Hermitian Hamiltonian for cavities coupled to a bath can be written as

$$H_{\text{eff}} = H_0 - \frac{i}{2} \mathbf{L}^\dagger \mathbf{\Gamma} \mathbf{L}, \quad (\text{S9})$$

where $\mathbf{L} = \begin{pmatrix} \hat{a}_1 \\ \hat{a}_2 \end{pmatrix}$. The effective Hamiltonian in Eq. S9 can be written in the following form

$$\hat{H}_{\text{eff}} = H_0 - \frac{i}{2} \begin{pmatrix} \hat{a}_c^\dagger & \hat{a}_y^\dagger \end{pmatrix} \begin{pmatrix} \kappa_c & 2iJ \\ 2iJ e^{-i\phi} & \kappa_y \end{pmatrix} \begin{pmatrix} \hat{a}_c \\ \hat{a}_y \end{pmatrix} \quad (\text{S10})$$

We can see that the diagonal terms give us a loss that makes oscillator frequencies complex, and the off-diagonal terms give us the desired nonreciprocal coupling. Any non-Hermitian Hamiltonian can be written as a sum of a Hermitian and an anti-Hermitian matrix[11]. To do so, consider a **non-Hermitian Hamiltonian** operator $\hat{H} \neq \hat{H}^\dagger$, which determines the time evolution of an arbitrary quantum observable $\hat{\chi}$ via the commutator:

$$i \frac{d\hat{\chi}}{dt} = [\hat{\chi}, \hat{H}]. \quad (\text{S11})$$

This commutator can be expressed in matrix form as:

$$i \frac{d\hat{\chi}}{dt} = [\hat{\chi} \quad \hat{H}] \begin{bmatrix} 0 & 1 \\ -1 & 0 \end{bmatrix} \begin{bmatrix} \hat{\chi} \\ \hat{H} \end{bmatrix}. \quad (\text{S12})$$

Here, the **symplectic matrix** is defined as:

$$\Omega = \begin{bmatrix} 0 & 1 \\ -1 & 0 \end{bmatrix}. \quad (\text{S13})$$

For compact notation, we define the **column vector**:

$$\chi_{\hat{H}} = \begin{bmatrix} \hat{\chi} \\ \hat{H} \end{bmatrix}. \quad (\text{S14})$$

The above equation can be written in the form

$$i \frac{d\chi}{dt} = \chi^T H \Omega \chi = [\chi(t), H]_{\Omega} \quad (\text{S15})$$

The above equation demonstrates the equivalence of this matrix structure concerning the commutator, establishing a Lie bracket and Lie algebra framework in quantum mechanics. By emphasizing the role of the matrix Ω , it suggests that alternative algebras and brackets can be constructed. This motivates the decomposition of any generic non-hermitian Hamiltonian into hermitian and anti-hermitian parts. The generic non-Hermitian Hamiltonian can always be decomposed into its **Hermitian** and **anti-Hermitian** components:

$$\hat{H} = \hat{H}_+ + \hat{H}_-, \quad (\text{S16})$$

where

$$\hat{H}_+ = \frac{\hat{H} + \hat{H}^\dagger}{2}, \quad \hat{H}_- = \frac{\hat{H} - \hat{H}^\dagger}{2i}. \quad (\text{S17})$$

The **commutator** with the non-Hermitian Hamiltonian splits into two parts

$$[\hat{\chi}, \hat{H}] = [\hat{\chi}, \hat{H}_+] + [\hat{\chi}, \hat{H}_-]. \quad (\text{S18})$$

From these equations, the **equation of motion for the density matrix** emerges [11], incorporating both the commutator and the anti-commutator:

$$\frac{d\hat{\rho}(t)}{dt} = -i[\hat{H}_+, \hat{\rho}(t)] + \{i\hat{H}_-, \hat{\rho}(t)\}_+, \quad (\text{S19})$$

where $\{\dots, \dots\}_+$ denotes the **anticommutator**. The above equation resembles the Lindblad master equation, but notice that the dissipation function is given by an anti-commutator term that contains the anti-Hermitian part of the Hamiltonian [11]. In the classical limit, the above equations of motion can be expressed as below:

$$\begin{bmatrix} \dot{q} \\ \dot{p} \end{bmatrix} = \Omega^{-1} \nabla H - \mathbf{G}^{-1} \nabla \Sigma, \quad (\text{S20})$$

where the dynamical equation is described in terms of two mathematical objects and their associated flows.

Here, Ω is the symplectic unit matrix, and \mathbf{G} is the phase space metric that describes the Euclidean geometry of phase space. The second flow is the canonical metric gradient flow, which arises from the imaginary part, Σ , of the Hamiltonian function. This flow represents the dissipative aspect of the dynamics, where energy gradients drive the evolution, and it is crucial for systems with non-conservative forces or open quantum systems. In the semi-classical limit, the creation and annihilation operators can be replaced by amplitudes, and the corresponding coupled equations of motion have the following form.

$$\frac{d}{dt} \begin{pmatrix} \alpha_c \\ \alpha_y \end{pmatrix} = \begin{pmatrix} -i(\omega_c - \omega_d - i\frac{\kappa_c}{2}) & -iJ \\ -iJ e^{i\phi} & -i(\omega_y - \omega_d - i\frac{\kappa_y}{2}) \end{pmatrix} \begin{pmatrix} \alpha_c \\ \alpha_y \end{pmatrix} + \begin{pmatrix} u_c \\ u_y \end{pmatrix}. \quad (\text{S21})$$

The two-by-two matrix in Eq. S21 is the dynamical matrix used for further analysis in the linear regime. We can also derive the same equations of motion by directly applying the Heisenberg equations of motion to an effective non-Hermitian Hamiltonian. The above dynamical matrix can also be obtained by introducing an intermediate third-mode approach, as shown in this reference [12].

D. Petermann Factor Analysis

The dynamical system model used in the text is given by

$$\tilde{\mathbf{A}} = \begin{bmatrix} -i(\tilde{f}_c - \tilde{f}_d) - \frac{\tilde{\kappa}_c}{2} & -i \\ -i e^{i\phi} & -i(\tilde{f}_c - \tilde{f}_d - \tilde{\Delta}_f) + (\tilde{\Delta}_\kappa - \frac{\tilde{\kappa}_c}{2}) \end{bmatrix} \quad (\text{S22})$$

The Petermann noise factor is defined as $K_{j'j} = \langle L_{j'} | L_j \rangle \langle R_j | R_{j'} \rangle$, where $\langle L_j |$ and $| R_j \rangle$ denote the left and right eigenvectors of $\tilde{\mathbf{A}}$ [13, 14]. For convenience, we use the mean diagonal Petermann noise factor $\bar{K}_2 = \frac{1}{2}(K_{11} + K_{22})$, whose deviation from unity measures eigenvector non-orthogonality and diverges at EPs [15]. While originally formulated to describe excess spontaneous emission in unstable lasers [13], the Petermann noise factor now serves more generally as a predictor of noise enhancement in non-Hermitian systems [16, 17]. To compute an analytical equation for \bar{K}_2 , we closely follow an example computation from [14]. First, we compute the eigenprojectors P_\pm using

$$P_\pm = - \oint_{C_\pm} \frac{dz}{2\pi i} R(z) = \text{Res}_{z=\lambda_\pm} R(z) \quad (\text{S23})$$

Here $R(z) = (\tilde{\mathbf{A}} - zI)^{-1}$. To compute P_\pm , we use symbolic residue calculation in MATLAB Symbolic Math Toolbox. Sample code is provided below

```
1 syms z
2 Rz = inv( Aeff - z*eye(2) );
3 P1 = -series(Rz, z, eigs(1), 'Order', 2) * (z - eigs(1));
4 P2 = -series(Rz, z, eigs(2), 'Order', 2) * (z - eigs(2));
```

Listing 1: Symbolic Residue Calculations

Where \mathbf{A} is defined symbolically outside of this code block, and $\text{eigs}(1) = \tilde{\lambda}_+$, $\text{eigs}(2) = \tilde{\lambda}_-$. This code uses the `series` function from the MATLAB Symbolic Math Toolbox to compute a Puiseux series expansion of the resolvent $R(z)$ around each eigenvalue, to first order (note, syntax is `n+1`). In this case, the expansion reduces to a standard Laurent series with integer powers. The spectral projector P_\pm is given by the residue at $z = \tilde{\lambda}_\pm$, which corresponds to the coefficient of the $(z - \tilde{\lambda}_\pm)^{-1}$ term. Multiplying the truncated series by $(z - \tilde{\lambda}_\pm)$ cancels the pole, leaving just the numerator of the singular term, the residue itself. We can then compute the mean of the diagonal Petermann factor

$$\bar{K}_2 = \frac{1}{2}(\|P_+\|_2^2 + \|P_-\|_2^2), \quad (\text{S24})$$

where $||M||_2 = \sqrt{\text{Tr}(M^\dagger M)}$ refers to the Frobenius (Hilbert-Schmidt) matrix norm. This yields the final equation for \bar{K}_2 , given in the Main Text as

$$\bar{K}_2 = \frac{\tilde{\Delta}_f^2 + \tilde{\Delta}_\kappa^2 + |\tilde{\Delta}_\lambda|^2 + 4}{2|\tilde{\Delta}_\lambda|^2}. \quad (\text{S25})$$

E. Cube Roots and TPDs

In this section, we provide additional information about how the peak extrema are analyzed in order to find TPDs. In the main text, we report the following cubic equation used to analyze the transmission spectrum $\tilde{\beta}_{ss}$ as

$$0 = f^3 + \tilde{p}f + \tilde{q}, \quad (\text{S26})$$

$$\tilde{p} = \frac{(\tilde{\kappa}_c - \tilde{\Delta}_\kappa)^2 + \text{Re}(\tilde{\Delta}_\lambda^2)}{4}, \quad (\text{S27})$$

$$\tilde{q} = \frac{(\tilde{\kappa}_c - \tilde{\Delta}_\kappa) \text{Im}(\tilde{\Delta}_\lambda^2)}{8}. \quad (\text{S28})$$

The three roots of Eq. S26 are the critical points of $\tilde{\beta}_{ss}$ and, remarkably, are related to the eigenspectrum of $\tilde{\mathbf{A}}$.

When Eq. S26 admits three real roots, the outermost roots (the largest and smallest), denoted $\tilde{\nu}_\pm^{\text{Root}}$, are used to find the transmission peak locations, while the intermediate root, denoted $\tilde{\eta}^{\text{Root}}$, is used to find the local minimum between the two peaks. When there is no splitting, Eq. S26 admits one real root, denoted $\tilde{\nu}_0^{\text{Root}}$, corresponding to the single peak frequency. Solving Eq. S26 for a closed form solution of the roots in terms of p, q can either be done using Cardano's method, which involves square and cube roots, or through a trigonometric solution first posed by François Viète in 1615 [18–20], which yields a solution for $\tilde{\nu}_\pm^{\text{Root}}$ as

$$\tilde{\nu}_\pm^{\text{Root}} = 2\sqrt{\frac{-\tilde{p}}{3}} \cos\left(\tilde{\theta} \pm \frac{\pi}{3}\right), \quad (\text{S29})$$

$$\tilde{\theta} = \frac{\pi}{3} + \frac{1}{3} \arccos\left(\frac{3\tilde{q}}{2\tilde{p}} \sqrt{\frac{-3}{\tilde{p}}}\right), \quad (\text{S30})$$

and a solution for $\tilde{\eta}^{\text{Root}}$ given by

$$\tilde{\eta}^{\text{Root}} = 2\sqrt{\frac{-\tilde{p}}{3}} \cos(\tilde{\theta}). \quad (\text{S31})$$

The expression for the splitting between the two peaks, $\tilde{\Delta}_\nu^{\text{Root}} = \tilde{\nu}_+^{\text{Root}} - \tilde{\nu}_-^{\text{Root}}$, admits a compact expression in terms of $\tilde{\theta}$ in Eq. S30 as

$$\tilde{\Delta}_\nu^{\text{Root}} = -2\sqrt{-\tilde{p}} \sin(\tilde{\theta}). \quad (\text{S32})$$

Equations S29 and S32 are undefined at $p = 0$, and are otherwise only valid in regions where the discriminant, expressed algebraically as

$$\text{Disc} \equiv_{\text{algebraic}} -4\tilde{p}^3 - 27\tilde{q}^2, \quad (\text{S33})$$

is positive, signifying three real root solutions to Eq. S26. In contrast, when $\text{Disc} < 0$, Eq. S29 and S32 are invalid, as there is only one real root, $\tilde{\nu}_0^{\text{Root}}$, given by

$$\tilde{\nu}_0^{\text{Root}} = \begin{cases} -2\frac{|\tilde{q}|}{\tilde{q}} \sqrt{\frac{-\tilde{p}}{3}} \cosh\left[\frac{1}{3} \text{arcosh}\left(\frac{-3|\tilde{q}|}{2\tilde{p}} \sqrt{\frac{-3}{\tilde{p}}}\right)\right], & \text{if } \tilde{p} < 0, \\ -2\sqrt{\frac{\tilde{p}}{3}} \sinh\left[\frac{1}{3} \text{arsinh}\left(\frac{3\tilde{q}}{2\tilde{p}} \sqrt{\frac{3}{\tilde{p}}}\right)\right], & \text{if } \tilde{p} > 0. \end{cases} \quad (\text{S34})$$

Naturally, the condition $\text{Disc} = 0$ marks the boundary between the single-peak and split-peak regimes. This boundary can be represented as a zero-contour in the $\tilde{\Delta}_f$ - $\tilde{\Delta}_\kappa$ plane, plotted in the Main Text. However, $\text{Disc} = 0$ alone does not define

the locations of TPDs, as it is not guaranteed that $\tilde{\Delta}_\nu^{\text{Root}} \rightarrow 0$ at $\text{Disc} = 0$. This can be illuminated through the geometric representation of the discriminant

$$\text{Disc} \equiv_{\text{geometric}} (r_1 - r_2)^2 (r_2 - r_3)^2 (r_3 - r_1)^2, \quad (\text{S35})$$

where r_1, r_2, r_3 are the roots of Eq. S26. For $\text{Disc} < 0$, one of the roots is real, given by $\tilde{\nu}_0^{\text{Root}}$, and the other two roots are a complex conjugate pair, not considered here. For $\text{Disc} > 0$, r_1, r_2, r_3 are $\tilde{\nu}^{\text{Root}}$, $\tilde{\eta}^{\text{Root}}$, $\tilde{\nu}_+^{\text{Root}}$ respectively. Finally, at $\text{Disc} = 0$, a multi-root degeneracy occurs, corresponding to the coalescence of either $\tilde{\nu}_+^{\text{Root}}$ or $\tilde{\nu}_-^{\text{Root}}$ with the central root $\tilde{\eta}^{\text{Root}}$, but not necessarily all three required for a TPD.

To differentiate between $\text{Disc} = 0$ causing a double-root degeneracy or a true TPD, an additional condition is required. In Eq. S33, enforcing $\text{Disc} = 0$ and $\tilde{q} = 0$ causes $\tilde{p} = 0$ as well. Then, $\tilde{p} = \tilde{q} = 0$ simplifies Eq. S26 to $f^3 = 0$, a triple degeneracy. Thus, TPDs occur precisely at intersections of the zero contours defined by $\text{Disc} = 0$ and $\tilde{q} = 0$, which are plotted in the Main Text.

F. Parameterization of TPD Surface

Here, we provide the full parameterization of the surface of TPDs surveyed in the Main Text. For $\phi = 0$, there are two TPDs along the $\tilde{\Delta}_\kappa$ axis as long as $\tilde{\kappa}_c^2 \leq 8$, located at $\frac{\tilde{\kappa}_c}{2} \pm \frac{\sqrt{8 - \tilde{\kappa}_c^2}}{2}$. When $\tilde{\kappa}_c \geq 2$, four more TPDs appear, with locations $(\tilde{\Delta}_\kappa, \tilde{\Delta}_f) = (0, \pm\sqrt{\tilde{\kappa}_c^2 - 4})$, and $(\tilde{\Delta}_\kappa, \tilde{\Delta}_f) = (\tilde{\kappa}_c, \pm\sqrt{\tilde{\kappa}_c^2 - 4})$. For $\phi = \pi$, there are always four TPDs, located at $(\tilde{\Delta}_\kappa, \tilde{\Delta}_f) = (0, \pm\sqrt{\tilde{\kappa}_c^2 + 4})$, and rogue TPDs located at $(\tilde{\Delta}_\kappa, \tilde{\Delta}_f) = (\tilde{\kappa}_c, \pm\sqrt{\tilde{\kappa}_c^2 + 4})$. For all other values of ϕ , the locations of the TPDs requires solving the following expression given by

$$\tilde{\Delta}_f = -\frac{-\tilde{\kappa}_c^2 x + 2\tilde{\kappa}_c x^2 - 2x^3 + 4\cos(\phi)x}{2\sin(\phi)}, \quad (\text{S36})$$

$$\tilde{\Delta}_\kappa = x, \quad (\text{S37})$$

$$x = \text{roots}(2x^4 - 2\tilde{\kappa}_c x^3 - x^2(4\cos(\phi) - \tilde{\kappa}_c^2) + 4\cos(\phi)^2 - 4) \quad (\text{S38})$$

where the roots operation refers to finding only the roots of the quartic equation without an imaginary component. Furthermore, there are two rogue TPDs at $(\tilde{\Delta}_\kappa, \tilde{\Delta}_f) = (\tilde{\kappa}_c, \pm\sqrt{\tilde{\kappa}_c^2 - 4\cos(\phi)})$.

G. Coupled Transmission Equation

The full equation for T_{Coupled} , used to find peak locations for experimental data, is given by

$$T_{\text{Coupled}} = \frac{16}{A^2 + B^2}, \quad (\text{S39})$$

with

$$A = 4\cos(\phi) - 4\tilde{f}_c^2 + 8\tilde{f}_c\tilde{f}_d + 4\tilde{\Delta}_f\tilde{f}_c - 4\tilde{f}_d^2 - 4\tilde{\Delta}_f\tilde{f}_d + \tilde{\kappa}_c^2 - 2\tilde{\Delta}_\kappa\tilde{\kappa}_c, \quad (\text{S40})$$

$$B = 4\sin(\phi) - 4\tilde{\Delta}_\kappa\tilde{f}_c + 4\tilde{\Delta}_\kappa\tilde{f}_d - 2\tilde{\Delta}_f\tilde{\kappa}_c + 4\tilde{f}_c\tilde{\kappa}_c - 4\tilde{f}_d\tilde{\kappa}_c. \quad (\text{S41})$$

H. Geometric Interpretation of Peaks and Imaginary Eigenvalues

Here, we include an additional perspective on the interpretation of peak locations, eigenvalues, EPs, and TPDs. There are special conditions for $\tilde{\kappa}_c$ such that EPs and TPDs coalesce into an EP-TPD pair. In Fig. 1, we show that these conditions occur for $\phi = 0$ at $\tilde{\kappa}_c = 2$ (Fig. 1c), and for $\phi = \pi$ at $\tilde{\kappa}_c = 0$ (Fig. 1e). However, for all other $\tilde{\kappa}_c$, the locations of TPDs, EPs, $\tilde{\nu}_\pm$, and $|\text{Im}(\tilde{\lambda}_\pm)|$ are all distinct. In particular, for $\phi = 0$, $\tilde{\nu}_\pm$ form ellipses whose semi-major ($\tilde{\Delta}_\kappa$) and semi-minor (frequency) axes scale with $\tilde{\kappa}_c$, while the ellipses formed by $|\text{Im}(\tilde{\lambda}_\pm)|$ stay constant with $\tilde{\kappa}_c$, providing a bound on $\tilde{\nu}_\pm$. For $\phi = \pi$, $\tilde{\nu}_\pm$ and $|\text{Im}(\tilde{\lambda}_\pm)|$ form hyperbolae, where the $\tilde{\nu}_\pm$ hyperbolae vertices drift outwards with $\tilde{\kappa}_c$.

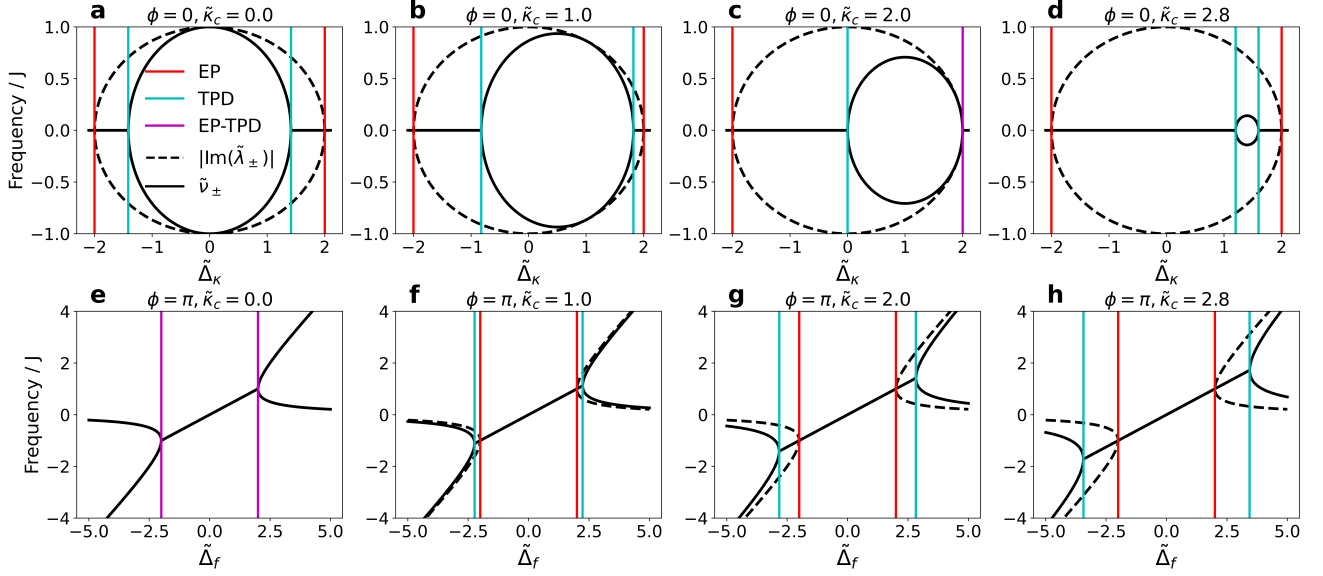


FIG. 1: **Geometry of Peak Locations and Imaginary Eigenvalues.** Geometric interpretation of the $\phi = 0$ and $\phi = \pi$ configurations. The imaginary eigenvalues, $|\text{Im}(\lambda_{\pm})|$ do not change with $\tilde{\kappa}_c$, while the peak locations, $\tilde{\nu}_{\pm}$, do.

I. Effect of Drive and Readout Vector on Peak Locations

In the Main Text, we only consider the drive/readout configuration of driving the cavity $\mathbf{B} = [1, 0]^T$ and reading the YIG $\mathbf{C} = [0, 1]$. We choose this configuration because the peak roots $\tilde{\nu}_{\pm}^{\text{Root}}$ are exactly solvable for the coupled transmission Eq. S39, which is not the case for other drive and readout configurations. Figure 2 displays the results of simulations for alternate drive and readout configurations for $\tilde{\kappa}_c = 2$. We show that the geometric intuition displayed in Fig. 1 does not hold for other drive/readout configurations. In particular, the drive/readout cavity configuration ($\mathbf{B} = [1, 0]^T$, $\mathbf{C} = [1, 0]$) admits two TPDs for $\phi = 0$ (Fig. 2b), with TPD locations not predicted by the Main Text theory. This drive/readout configuration does not admit any TPDs for the $\phi = \pi$ configuration (Fig. 2e). For the drive/readout YIG configuration, $\phi = 0$ admits one TPD (Fig. 2c), $\phi = \pi$ admits zero (Fig. 2f).

II. EXPERIMENTAL DETAILS

A. YIG Ferromagnetic Resonance

Although YIG is technically ferrimagnetic, we ensure the material is driven into magnetic saturation. In this regime, the net magnetization precesses uniformly, and the standard ferromagnetic formalism can accurately describe its dynamics. Thus, the Larmor frequency precesses linearly on the applied field as $f_y = \mu_B B_z / 2\pi$, where μ_B is the Bohr magneton, consistent with the simplified Kittel formula for a uniformly magnetized sphere [21]. Several factors ensure the validity of this approximation. First, the saturation magnetization of our YIG sample is $\mu_0 M_s = 0.178$ T, and we apply a bias field exceeding this value using permanent neodymium magnets. Second, the YIG sample is spherical, eliminating shape-dependent demagnetization effects since the demagnetization factors are isotropic ($N_x = N_y = N_z = 1/3$) [22]. Third, thermal effects can be neglected in our regime, as the Curie temperature of YIG ($\sim 560^\circ\text{K}$) [23] is far above our room temperature operating conditions.

B. Device Schematics

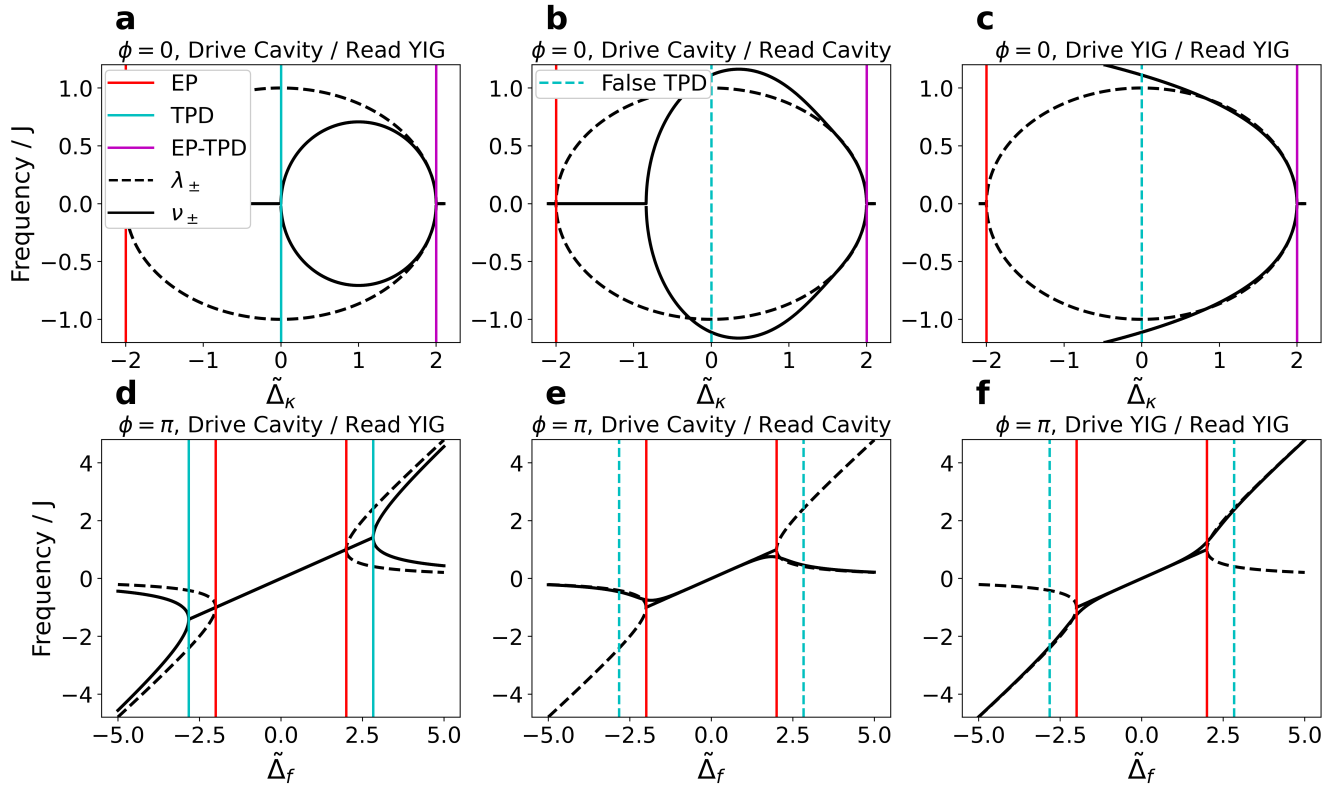


FIG. 2: Drive Configuration and Peak Locations. Simulations of ν_\pm for $\kappa_c/J = 2$. **a(d)** depicts drive cavity, readout YIG $\mathbf{B} = [1, 0]^T$, $\mathbf{C} = [0, 1]$ for $\phi = 0$ ($\phi = \pi$), where theory presented in the Main Text holds. **b(e)** depicts drive/readout cavity configuration $\mathbf{B} = [1, 0]^T$, $\mathbf{C} = [1, 0]$ for $\phi = 0$ ($\phi = \pi$). **c(f)** depicts drive/readout YIG configuration $\mathbf{B} = [0, 1]^T$, $\mathbf{C} = [0, 1]$ for $\phi = 0$ ($\phi = \pi$). Dashed cyan lines depict mismatch between Main Text theory and alternate drive vectors.

-
- [1] Y.-P. Wang and C.-M. Hu, Dissipative couplings in cavity magnonics, *Journal of Applied Physics* **127**, 130901 (2020), https://pubs.aip.org/aip/jap/article-pdf/doi/10.1063/1.5144202/20002098/130901_1_1.5144202.pdf.
 - [2] K. Fang, J. Luo, A. Metelmann, M. H. Matheny, F. Marquardt, A. A. Clerk, and O. Painter, Generalized non-reciprocity in an optomechanical circuit via synthetic magnetism and reservoir engineering, *Nature Physics* **13**, 465 (2017), publisher: Nature Publishing Group.
 - [3] Y.-P. Wang, J. W. Rao, Y. Yang, P.-C. Xu, Y. S. Gui, B. M. Yao, J. Q. You, and C.-M. Hu, Nonreciprocity and Unidirectional Invisibility in Cavity Magnonics, *Physical Review Letters* **123**, 127202 (2019), publisher: American Physical Society.
 - [4] N. R. Bernier, L. D. Tóth, A. K. Feofanov, and T. J. Kippenberg, Level attraction in a microwave optomechanical circuit, *Physical Review A* **98**, 023841 (2018), publisher: American Physical Society.
 - [5] R. Wen, C.-L. Zou, X. Zhu, P. Chen, Z. Y. Ou, J. F. Chen, and W. Zhang, Non-hermitian magnon-photon interference in an atomic ensemble, *Phys. Rev. Lett.* **122**, 253602 (2019).
 - [6] A. Clerk, Introduction to quantum non-reciprocal interactions: from non-Hermitian Hamiltonians to quantum master equations and quantum feedforward schemes, *SciPost Physics Lecture Notes*, 044 (2022).
 - [7] B. Yao, T. Yu, X. Zhang, W. Lu, Y. Gui, C.-M. Hu, and Y. M. Blanter, The microscopic origin of magnon-photon level attraction by traveling waves: Theory and experiment, *Physical Review B* **100**, 214426 (2019), publisher: American Physical Society.
 - [8] A. Metelmann and A. A. Clerk, Nonreciprocal photon transmission and amplification via reservoir engineering, *Phys. Rev. X* **5**, 021025 (2015).
 - [9] Y.-P. Wang and C.-M. Hu, Dissipative couplings in cavity magnonics, *Journal of Applied Physics* **127**, 130901 (2020).
 - [10] Y. Shi, C. Zhang, Z. Hao, C. Jiang, C. K. Ong, K. Xia, and G. Chai, Nonreciprocal singularities dominated by the dissipative photon-magnon coupling in non-hermitian systems (2024), [arXiv:2405.17869 \[cond-mat.mes-hall\]](https://arxiv.org/abs/2405.17869).
 - [11] E.-M. Graefe, M. Höning, and H. J. Korsch, Classical limit of non-hermitian quantum dynamics—a generalized canonical structure, *Journal of Physics A: Mathematical and Theoretical* **43**, 075306 (2010).
 - [12] J. Rohn, K. P. Schmidt, and C. Genes, Classical phase synchronization in dissipative non-hermitian coupled systems, *Phys. Rev. A* **108**, 023721 (2023).
 - [13] A. E. Siegman, Excess spontaneous emission in non-Hermitian optical systems. II. Laser oscillators, *Physical Review A* **39**, 1264 (1989), publisher: American Physical Society.

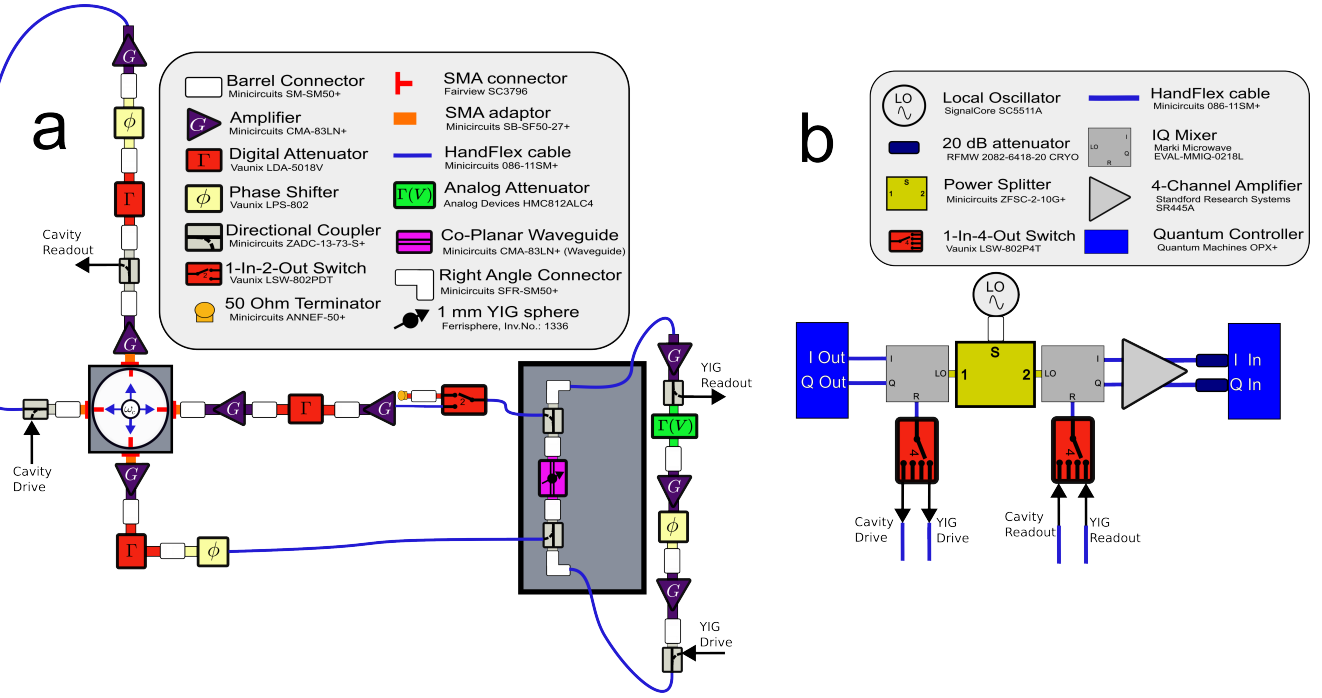


FIG. 3: **Schematic for tunable magnon-photon dimer.** Closed-loop configuration of coupled cavity and YIG mode, including switches to change between drive/readout operating modes, self-feedback loops, and all experimental devices. All active devices, except for the amplifier, are controlled using a Python API.

- [14] Y. Ashida, Z. Gong, and M. Ueda, Non-Hermitian Physics, *Advances in Physics* **69**, 249 (2020), arXiv:2006.01837 [cond-mat].
- [15] M. C. Zheng, D. N. Christodoulides, R. Fleischmann, and T. Kottos, \mathcal{PT} optical lattices and universality in beam dynamics, *Physical Review A* **82**, 010103 (2010), publisher: American Physical Society.
- [16] H. Wang, Y.-H. Lai, Z. Yuan, M.-G. Suh, and K. Vahala, Petermann-factor sensitivity limit near an exceptional point in a Brillouin ring laser gyroscope, *Nature Communications* **11**, 1610 (2020), publisher: Nature Publishing Group.
- [17] S. Ghosh, A. Roy, S. Dey, B. P. Pal, and S. Ghosh, Suppression of the Petermann noise factor in a chiral optical mode converter without encircling an exceptional point, *JOSA B* **41**, 2534 (2024), publisher: Optica Publishing Group.
- [18] R. W. D. Nickalls, Viète, Descartes and the cubic equation, *The Mathematical Gazette* **90**, 203 (2006).
- [19] G. C. Holmes, The use of hyperbolic cosines in solving cubic polynomials, *The Mathematical Gazette* **86**, 473 (2002).
- [20] F. Viète, Ad Angularum Sectionem Analytica Theoremata, *Opera mathematica* **volume 4** (1615).
- [21] M. Sparks, R. Loudon, and C. Kittel, Ferromagnetic Relaxation. I. Theory of the Relaxation of the Uniform Precession and the Degenerate Spectrum in Insulators at Low Temperatures, *Physical Review* **122**, 791 (1961), publisher: American Physical Society.
- [22] J. A. Osborn, Demagnetizing Factors of the General Ellipsoid, *Physical Review* **67**, 351 (1945), publisher: American Physical Society.
- [23] D. Zhang, X.-M. Wang, T.-F. Li, X.-Q. Luo, W. Wu, F. Nori, and J. Q. You, Cavity quantum electrodynamics with ferromagnetic magnons in a small yttrium-iron-garnet sphere, *npj Quantum Information* **1**, 1 (2015), publisher: Nature Publishing Group.